CORONAL OBSERVATIONS OF CMEs
Report of Working Group A

R. SCHWENN[1,*], J. C. RAYMOND[2], D. ALEXANDER[3], A. CIARAVELLA[1,4],
N. GOPALSWAMY[5], R. HOWARD[6], H. HUDSON[7], P. KAUFMANN[8,9],
A. KLASSEN[10], D. MAIA[11], G. MUNOZ-MARTINEZ[12], M. PICK[13], M. REINER[5],
N. SRIVASTAVA[14], D. TRIPATHI[1], A. VOURLIDAS[6], Y.-M. WANG[6] and J. ZHANG[5]

[1]*Max-Planck-Institut für Sonnensystemforschung Katlenburg-Lindau, Germany*
[2]*Center for Astrophysics, Cambridge, MA, USA*
[3]*Dept. of Physics and Astronomy, Rice University, Houston, TX, USA*
[4]*INAF Osservatorio Astronomico di Palermo, Palermo, Italy*
[5]*School of Computational Sciences, George Mason University, Fairfax, VA, USA;*
NASA GSFC, Lab. for Extraterrestrial Physics, Greenbelt, MD, USA
[6]*US Naval Research Laboratory, Washington, DC, USA*
[7]*Space Sciences Laboratory, University of California, Berkeley, CA, USA*
[8]*Universidade Presbiteriana Mackenzie, CRAAM, Sao Paulo, SP, Brazil*
[9]*Universidade Estadual de Campinas, CCS, Campinas, SP, Brazil*
[10]*Astrophysikalisches Institut Potsdam, Potsdam, Germany*
[11]*CICGE, Observatório Astronómico Professor Manuel de Barros, Faculdade de Ciências da*
Universidade do Porto, Vila nova de Gaia, Portugal
[12]*Instituto de Geofísica, UNAM, Mexico*
[13]*LESIA, UMR 8109 CNRS, Observatoire de Paris, Meudon, France*
[14]*Udaipur Solar Observatory, Physical Research Laboratory, Udaipur, India*
*(*Author for correspondence, E-mail: schwenn@linmpi.mpg.de)*

Abstract. CMEs have been observed for over 30 years with a wide variety of instruments. It is now possible to derive detailed and quantitative information on CME morphology, velocity, acceleration and mass. Flares associated with CMEs are observed in X-rays, and several different radio signatures are also seen. Optical and UV spectra of CMEs both on the disk and at the limb provide velocities along the line of sight and diagnostics for temperature, density and composition. From the vast quantity of data we attempt to synthesize the current state of knowledge of the properties of CMEs, along with some specific observed characteristics that illuminate the physical processes occurring during CME eruption. These include the common three-part structures of CMEs, which is generally attributed to compressed material at the leading edge, a low-density magnetic bubble and dense prominence gas. Signatures of shock waves are seen, but the location of these shocks relative to the other structures and the occurrence rate at the heights where Solar Energetic Particles are produced remains controversial. The relationships among CMEs, Moreton waves, EIT waves, and EUV dimming are also cloudy. The close connection between CMEs and flares suggests that magnetic reconnection plays an important role in CME eruption and evolution. We discuss the evidence for reconnection in current sheets from white-light, X-ray, radio and UV observations. Finally, we summarize the requirements for future instrumentation that might answer the outstanding questions and the opportunities that new space-based and ground-based observatories will provide in the future.

1. Introduction

CMEs have been observed for over 30 years with a wide variety of instruments. White light coronagraphs in space provide the bulk of the observations. The examples shown in Figure 1 demonstrate how the capabilities of coronagraphs have developed over the years and the state of maturity they have reached. It is now possible to derive detailed and quantitative information on CME morphology, velocity, acceleration and mass.

Flares associated with CMEs are observed in white light, the Hα emission line, extreme ultraviolet light (EUV) and X-rays, and several different radio signatures are also seen. Optical and UV spectra of CMEs both on the disk and at the limb provide velocities along the line of sight and diagnostics for temperature, density and composition.

From the vast quantity of data available we attempt to synthesize the current state of knowledge of the properties of CMEs, along with some specific observed characteristics that illuminate the physical processes occurring during CME eruption. These include the common three-part structure of many CMEs, which is generally attributed to compressed material at the leading edge, a low density magnetic bubble and dense prominence gas. Signatures of shock waves are seen, but the locations of these shocks relative to the other structures and the occurrence rates at the heights where Solar Energetic Particles (SEPs) are produced remain controversial. The relationships among CMEs, Moreton waves, EIT waves (as discovered by the Extreme Ultraviolet Imaging Telescope on the Solar and Heliospheric Observatory, SOHO) and EUV dimming are also cloudy.

The close connection between CMEs and flares suggests that magnetic reconnection may play an important role in CME eruption and evolution. We discuss the evidence for reconnection in current sheets from white light, X-ray, radio and UV observations. Finally, we summarize the requirements for future instrumentation that might answer the outstanding questions and the opportunities that new space-based and ground-based observatories will provide in the near future.

2. Available Observations

2.1. SPACE-BASED CORONAGRAPHS

CMEs were discovered and have been mainly studied by space-based coronagraphs. Many observations described in this book were obtained by the Large Angle and Spectrometric Coronagraphs (LASCO; Brueckner *et al.*, 1995) operating aboard SOHO (Domingo *et al.*, 1995). LASCO is a wide-field white light and spectrometric coronagraph consisting of three optical systems having nested fields of view that together observe the solar corona from just above the limb at $1.1\,R_\odot$ out to very great
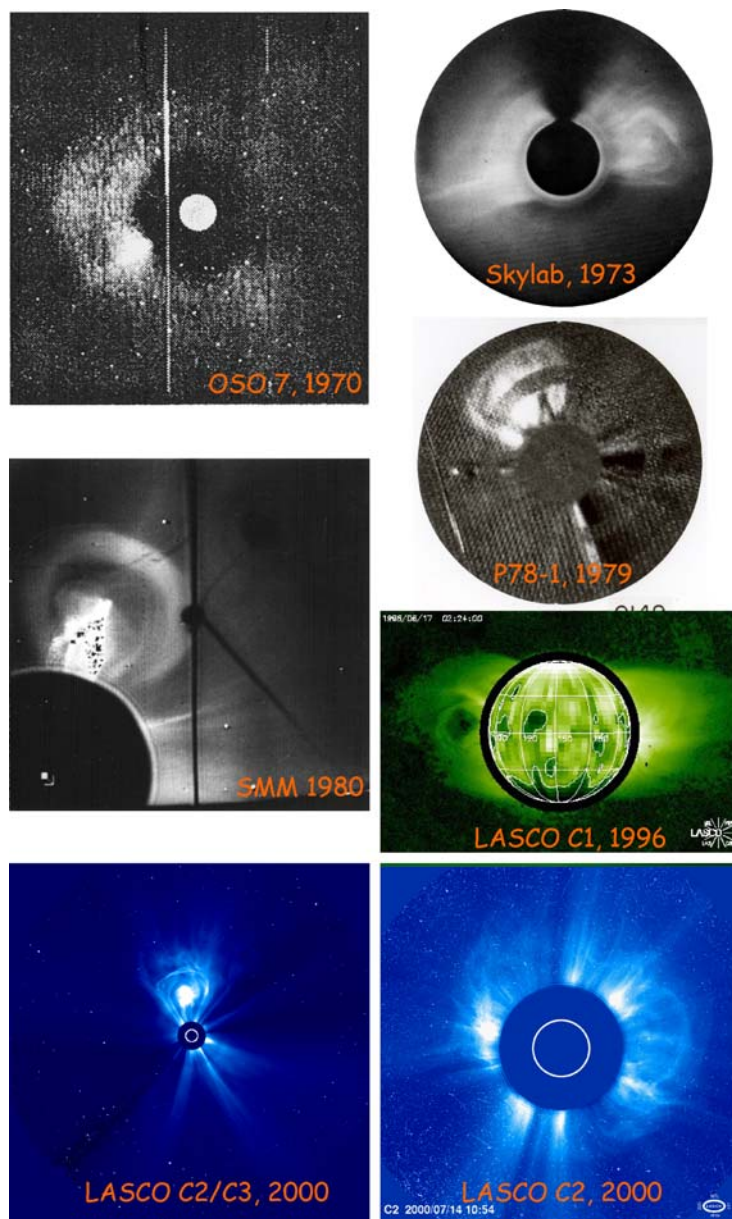
Figure 1. Examples of CME observations from space, from the first one (seen from OSO-7 on Dec. 14, 1971 by Brueckner *et al*. (1972, 1973)) to the still-ongoing LASCO. The lower right panel shows a "halo" CME pointed along the Sun-Earth line.

elongations. The three telescopes comprising LASCO are designated C1 (1.1 to 3.0 $R_\odot$), C2 (2.2 to 6.0 $R_\odot$) and C3, which spans the outer corona (4 to 32 $R_\odot$). C1 is fitted with an imaging Fabry-Perot interferometer, making possible spatially resolved high-resolution coronal spectroscopy in selected spectral lines. Unfortunately, C1 was severely damaged during the temporary loss of SOHO and no observations have been possible since June 1998. C2 and C3 mostly operate in synoptic mode at a cadence of about 24 min (C2) and 45 min (C3). The resolution is 11.9 arcsec/pix for C2 and 53 arcsec/pix for C3. Their observations have resulted in a database of about 10,000 CMEs (Yashiro *et al.*, 2004) as of mid 2005. Some characteristic examples are shown in Figure 1.

SOHO also carries another type of coronagraph, the Ultraviolet Coronagraph Spectrometer (UVCS; Kohl *et al.*, 1995). UVCS obtains long slit spectroscopic measurements of the corona at heights between 1.2 and 10 $R_\odot$ with 7 arcsec/pix resolution in a variety of lines (HI 1216 Å, OVI 1032, 1037 Å, Mg X 610/625 Å, Si XII 499/521 Å, Fe XII 1242 Å), and it also has a visible light channel. UVCS can rotate its field of view about Sun center to build maps of the full corona. Figure 2 shows a tomographic reconstruction of the coronal emission in the O VI $\lambda 1032$ line as seen from the Earth and as it would be seen if the Sun's axis were tilted by increments of 40° (Panasyuk, 1999).

2.2. GROUND-BASED CORONAGRAPHS

Ground-based coronagraphs complement the space-based coronagraphs. Although ground-based coronagraphs are limited by brightness and temporal variability of the sky, they allow a higher temporal resolution. This facilitates the understanding of the trigger mechanism of fast transient phenomena like CMEs and coronal waves in the lower corona as well as the density and temperature structure.

Ground-based white-light coronal observations can be obtained only for a small range of heliocentric heights and only with polarization measurements to remove most of the unpolarized sky background. Routine observations have been carried out at the Mauna Loa Solar Observatory (MLSO) for many years. The current coronagraph, Mark IV, has been operational since 1998. It records polarized brightness images of the corona from 1.08–2.85 $R_\odot$ every 3 minutes. The observations run from 17–22 UT daily (weather permitting). Mark IV complements nicely the LASCO observations by providing observations of the inner corona (Figure 3).

Finally, there are several ground-based spectroscopic coronagraph instruments operating within a single bandpass such as the Hα coronagraphs at Pic du Midi and MLSO, the [Fe XIV] and [Fe X] instruments in Sac Peak and Norikura solar observatories, the HeI coronagraph at MLSO, the MICA instrument in Argentina (Stenborg *et al.*, 2000) and some others.
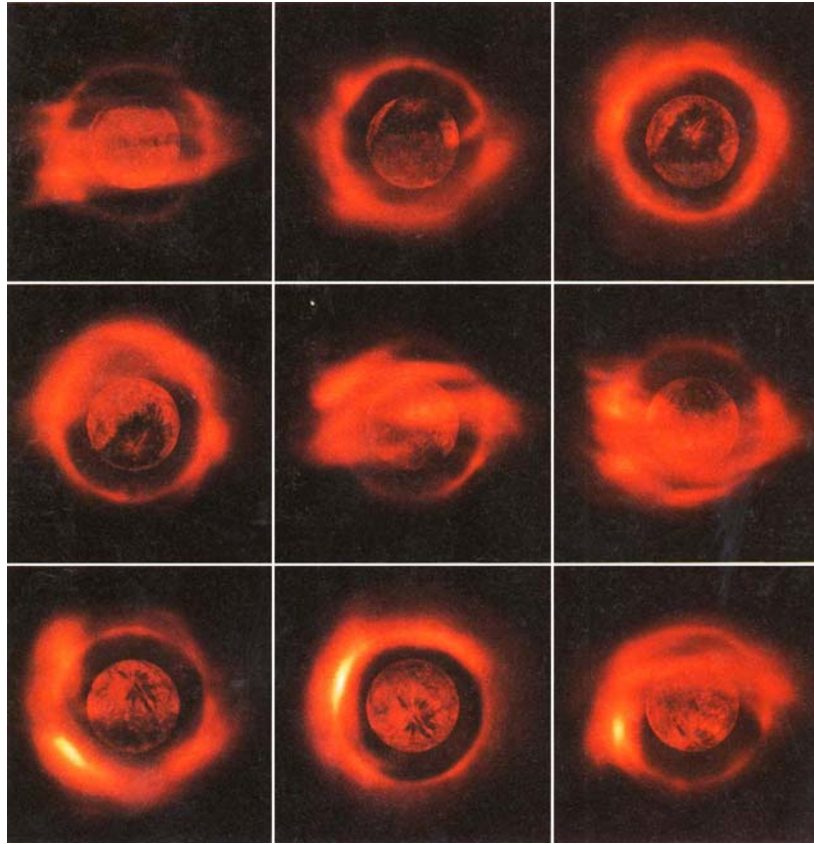
Figure 2. Tomographic reconstruction of the quiet Sun O VI λ1032 emissivity derived from UVCS observations during Whole Sun Month 1996 (Panasyuk, 1999). Successive panels left to right across each row show the corona as seen if the Sun's axis were tilted in the plane containing the Earth and the solar axis by increments of 40°. EIT brightness for this Carrington rotation is shown in the center.

2.3. EIT/TRACE, EUV Spectrographs

Since the launch of SOHO, EIT (Delaboudinière *et al.*, 1995) has provided almost continuous full Sun images with 2.6″ pixels in 4 narrow EUV bands. The four bands reveal structures primarily in Fe IX, Fe XII, Fe XV and He II, covering a temperature range 10^5 to 2×10^6 K. In some circumstances other ions may dominate, as when Fe XXIV appears in flares or O V becomes strong in CMEs. TRACE (Handy *et al.*, 1999) has higher spatial resolution, with 0.5″ pixels, providing images such as that in Figure 9, and a much higher time cadence. It has 3 EUV bands similar to those of EIT, along with UV bands. The SPIRIT experiment on CORONAS-F produces images in EUV bands similar to those of EIT, along with images in the Mg XII Lyα X-ray line (Zhitnik *et al.*, 2003a).
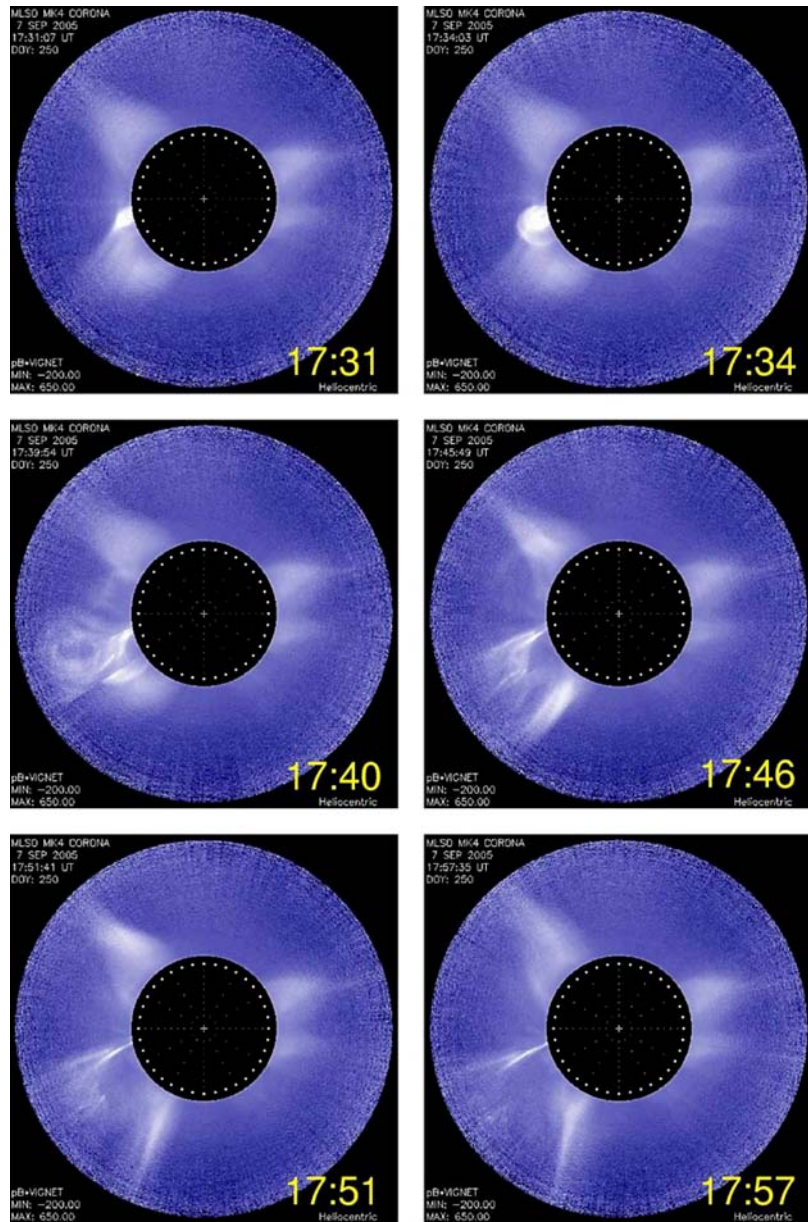
Figure 3. The big CME on September 7, 2005 as seen by the Mark IV coronagraph on Mauna Loa in Hawaii. The CME was accompanied by an X17 flare at S06E89 as reported by NOAA with a peak flux at 17:40. EIT and LASCO on SOHO were switched off because of an attitude maneuver. Despite the CME's origin at the east limb, the Earth was hit by a shock wave and a succeeding magnetic cloud that caused a Kp9 geomagnetic storm on September 11.

Three UV/EUV spectrographs currently operating are SUMER (Wilhelm *et al*., 1995) and CDS (Harrison *et al*., 1995) on the SOHO spacecraft and the SPIRIT experiment on CORONAS-F (Zhitnik *et al*., 2003b). These instruments observe spectral ranges from 151 to 1610 Å, providing many lines useful as temperature, density and abundance diagnostics.

2.4. MDI

The Michelson-Doppler Imager (MDI) is part of the SOHO Solar Oscillations Investigation (SOI; Scherrer *et al*., 1995). MDI provides full-Sun line-of-sight measurements of the photospheric magnetic field at $4''$ resolution with a typical cadence of 96 minutes. A high resolution partial-Sun field of view has a $1.25''$ resolution across a field-of view $11'$ wide. Such measurements at lower cadence and with less spatial resolution are also provided by ground-based observatories such as Kitt Peak National Observatory (near Tucson, USA) and Wilcox Solar Observatory (near Los Angeles, USA).

MDI has contributed successfully to the understanding of CME initiation and propagation by providing the necessary global magnetic field context within which the CMEs occur. Knowledge of the time variability and distribution of the magnetic field on the solar surface is required as boundary conditions for models of the global solar corona through which the CMEs propagate (e.g., Linker *et al*., 1999; Luhmann *et al*., 2003) and for input to MHD models of the eruption process.

2.5. Soft X-Ray Imaging

X-ray light curves from GOES are the standard means for comparing CME and flare characteristics, and imaging data provide still stronger constraints. Soft X-ray imaging of the solar corona began in 1960 via a primitive pinhole camera on a sounding rocket; by the 1970s routine rocket-borne focusing-optics telescopes led to the revolutionary imaging from Skylab (e.g. Vaiana *et al*., 1973). From 1991 the soft X-ray telescope SXT on *Yohkoh* began systematic CCD-based observations with excellent resolution, image cadence, and image dynamic range. Following *Yohkoh's* demise in 2001, the first NOAA soft X-ray imager (SXI on GOES-12; Hill *et al*., 2005) began observations, and a sequence of follow-on SXI instruments will continue on future GOES spacecraft. Solar-B (2006 launch) will have an advanced soft X-ray telescope.

The soft X-ray images, as opposed to EUV images, give us a more broadband view of the optically thin corona. Phenomena that are well-observed by these instruments include coronal holes, filament channels, active regions, microflares, X-ray bright points, X-ray dimmings, sigmoids, trans-equatorial loops, hot ejecta, X-ray jets, flare loops, loop-top brightenings, *above*-the-loop-top sources, supra-arcade

downflows, flare footpoints, Moreton-type shock fronts, and of course lovely flare arcades and spectacular cusp-shaped structures above them.

2.6. HARD X-RAY IMAGING

At energies above a few keV, focusing optics have thus far been difficult to implement. Only these hard X-rays, though, can properly reveal particle acceleration and energy release in the low corona. Accordingly HXIS (on SMM), SXT on (*Hinotori*), HXT (on *Yohkoh*) and RHESSI (Lin *et al.*, 2002) have resorted to shadow-mask imaging, to provide arc-second resolution for hard X-rays. In the case of RHESSI even some γ-ray imaging has been possible.

The new data reveal a broad range of coronal sources as well as the footpoint sources of the flare impulsive phase. All of these sources require particle acceleration to high energies, and the particle acceleration produces a hard X-ray signature characteristic of CME sources (Kiplinger, 1995). The non-thermal energy release turns out to dominate even the weakest microflares as well. The signatures of solar particle acceleration are sometimes accompanied by SEP events, giving us the possibility of thus directly identifying the solar origin of the interplanetary field lines containing the SEP particles. Finally, and surprisingly, the RHESSI data show that ions and electrons occupy *different* flaring loops.

2.7. GROUND-BASED EMISSION LINE OBSERVATIONS

From the ground, various features of mass ejections can be observed at visible and IR wavelengths. Such data help us to study in detail the pre-eruptive scenario to identify the chain of events and the conditions leading up to the eruption or the CME. A few important spectral lines include:

1. Hα: The Hα line has been used to record solar eruptions for a very long time. The lower chromosphere is the coolest layer in the Sun's atmosphere, and prominent features associated with solar activity such as flares and filaments are best observed in this line. In Hα images, the counterpart of the bright knot of the three part structure is observed, which corresponds to the features cooler than the frontal edge of the CMEs. Hα filaments on the disk are seen in absorption, but when they reach the solar limb and extend beyond it, they are seen in emission and are called prominences. When a filament in the course of a CME begins to rise, the Hα emission is Doppler shifted and may no longer be visible in narrow band images. These are the "Disappearing Filaments" (DFs; see Figure 4).
2. Ca II K: Because the Calcium K Line (393.3 nm) is sensitive to magnetic fields, magnetically active structures show up in high contrast against the surrounding chromosphere. Regions of moderate magnetic field appear bright, whereas high magnetic field regions are dark. In CaK images, one is able to see the brightness
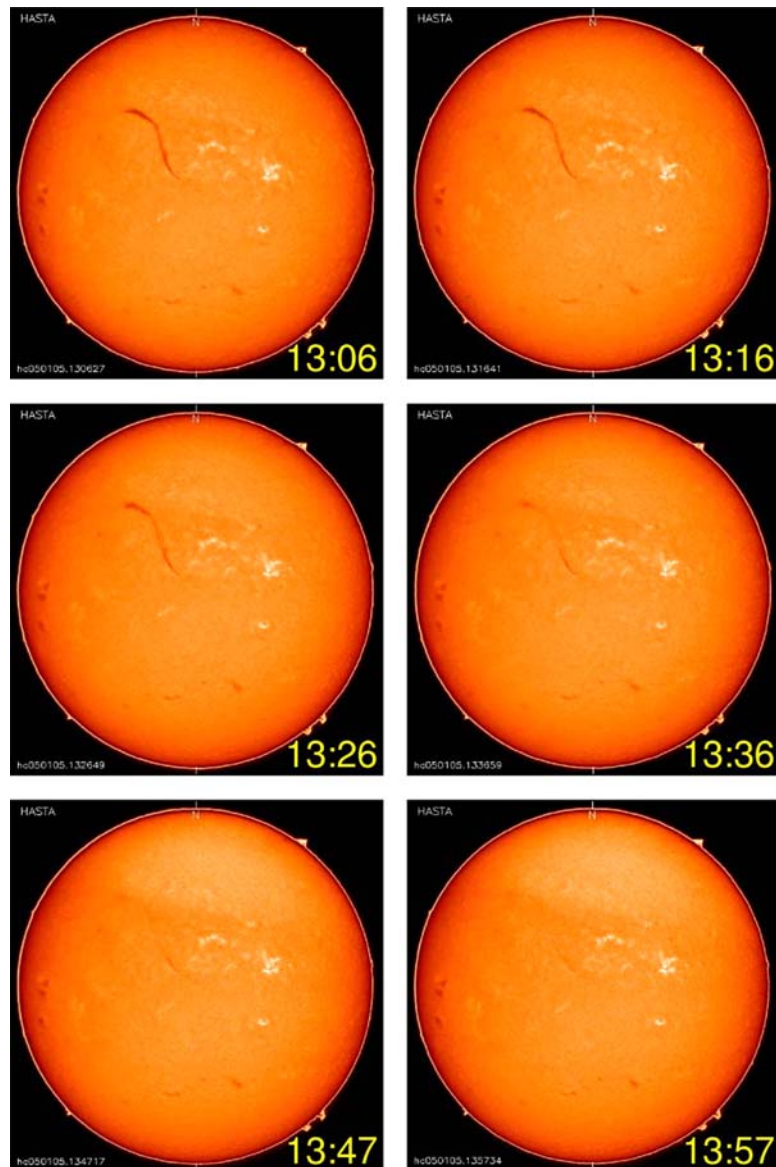
Figure 4. A disappearing filament in the northeast observed by the HASTA-telescope on January 5, 2005. It was associated with a minor X-ray brightening (B1.5) and a full halo CME. No associated shock was noted at the Earth, but a geomagnetic storm (Kp7) occurred late on January 7.

along the edges of large convection cells called supergranules and in areas called plages. Dark sunspots and filaments are also visible in this wavelength.

3. He 10830: The He 10830 line is very useful for indirect observations of the corona. The conditions in the overlying corona are mainly responsible for the

excitation of the chromospheric helium. Coronal holes are marginally detectable in this line and are mapped as somewhat brighter regions in He 1083.0 nm images (Harvey and Sheeley, 1979).

2.8. VECTOR MAGNETOGRAPHS

Vector magnetographs allow both the longitudinal and transverse components of the magnetic field to be measured, using the circular and linear polarization of magnetically-sensitive spectral lines in the solar photosphere and chromosphere. A number of vector magnetographs are currently operational around the world using a variety of lines including Fe I at 6301.5 Å and 6302.5 Å (Advanced Stokes Polarimeter, Skumanich *et al.*, 1997; Mees Imaging Vector Magnetograph, Mickey *et al.*, 1996) and Ca I at 6301 Å (Big Bear Solar Observatory Digital Vector Magnetograph, Spirock *et al.*, 2001) in the photosphere and Na I D at 5896 Å (Mees IVM, Metcalf *et al.*, 1995) in the chromosphere. Other facilities at MSFC, Potsdam, Huairou, Irkutsk, Udaipur and Mitaka result in almost continuous vector field coverage of the Sun.

The vector magnetographs currently in use typically have a field of view encompassing a single active region ($\sim 5' \times 5'$) with a pixel size of order $0.5''$ or greater and can generate a full magnetogram every 2–3 minutes. Uncertainties in the magnetic field tend to be of the order of 10–20 G in the longitudinal field and 25–50 G in the transverse field measurements. In addition, there is an $180°$ ambiguity issue in the transverse field measurements which is solved by a number of different means (e.g. Canfield *et al.*, 1993).

Knowledge of the full magnetic vector allows one to determine the size and nature of any currents in the system, as well as measures of twist and helicity. In particular, without knowledge of the vector magnetic field a quantitative assessment of the amount of "free energy" available in the corona to power an eruption would be impossible.

2.9. RADIOHELIOGRAPHS AND RADIO ARRAYS

The radio imaging instruments map the corona over a range of altitudes depending on the observing frequencies. They provide observations of prominences, microwave activity during flares, coronal and CME-driven shocks.

There are only a very few dedicated solar imaging instruments currently under operation. They include the Nobeyama Radioheliograph (NoRH; Nakajima *et al.*, 1994; 17 and 34 GHz), the Owens Valley Radio Observatory (OVRO; Gary and Hurford, 1990; 1–18 GHz), the Nançay Radioheliograph (NRH; Kerdraon and Delouis, 1997; 450–150 MHz), the Gauribidanour Radioheliograph (Ramesh *et al.*, 1998; 40–150 MHz), the Siberian Solar Radio Telescope (SSRT, Zandanov *et al.*, 1999; 5.7 GHz), and the Ratan-600 radio telescope (Bogod *et al.*, 1998) (610 MHz

– 30 GHz). Large non-solar dedicated arrays, such as the Very Large Array (VLA) (operating at microwave frequencies and more recently at 75 MHz) in the United States (Erickson *et al.*, 2000) and the Giant Meterwave Radiotelescope (GMRT) operating at 327 MHz, 236 MHz, 600 MHz and 1420 MHz (Rao *et al.*, 1995; Swarup, 2000) in India provide occasional observations.

2.10. SUBMILLIMETER-WAVE SOLAR RADIO ASTRONOMY

A new tool to observe the Sun in the submillimeter range of wavelengths has become available, operating on a daily basis since 2002 at El Leoncito observatory in the Argentina Andes (Kaufmann *et al.*, 2001). It has shown the association between the launch time of CMEs and the onset of the new kind of rapid subsecond pulsating bursts, discovered at 212 and 405 GHz (Kaufmann *et al.*, 2003).

3. CME Properties

White-light coronagraph images make it possible to derive the column density of CME plasma, and radio observations allow us to measure the density. Ultraviolet spectra from SUMER and UVCS provide the means to measure density, temperature, elemental composition and ionization state.

3.1. STATISTICAL PROPERTIES

CMEs are characterized by speed, angular width, acceleration, and a central position angle in the sky plane. Measured speeds range from a few km/s to nearly 3000 km/s (e.g., Gopalswamy, 2004; see also previous studies by Howard *et al.*, 1985 and St. Cyr *et al.*, 2000), with an average value of ∼450 km/s (see Figure 5), which is slightly higher than the slow solar wind speed. The apparent angular width of CMEs ranges from a few degrees to more than 120 degrees, with an average value of ∼47° (counting only CMEs with width less than 120°). The width and other parameters of a CME occurring close to the limb is likely to be the true width, whereas the width and source latitude of a CME occurring close to the disk center are severely affected by projection effects (Burkepile *et al.*, 2004). CME acceleration is discussed in Section 4.

3.1.1. *Mass and Energy*
The current LASCO database of CMEs (as of Fall 2005) contains more than 10000 events. CME observations are available over a significant part of a solar cycle, thereby allowing us to obtain a very reliable estimate of their mass and energy profiles. Such statistics for all events up to 2002 have been presented in Vourlidas *et al.* (2002). The measurement methods and assumptions used can also be found
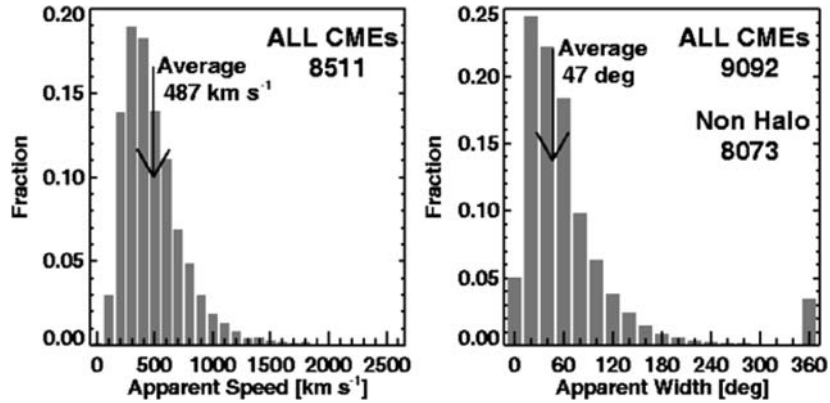
Figure 5. Speeds (left) and widths (right) of all CMEs observed by SOHO/LASCO from 1996 to the end of 2004 (Gopalswamy *et al.*, 2005b). The speed could not be measured for all the detected CMEs. The averages of the distributions are shown on the plots. The average width was computed from non-halo CMEs.
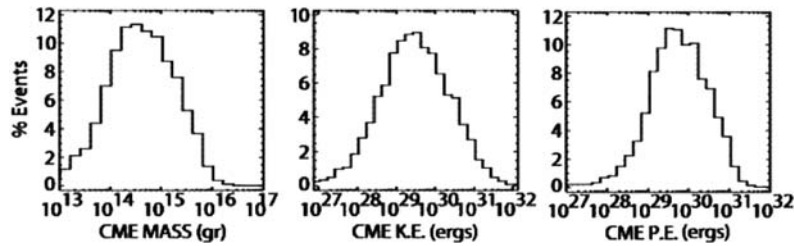

Figure 6. Statistics of mass and energy for 1996–2004 CMEs compiled by A. Vourlidas (6,335 events).

in the same paper. Here we update these statistics for all CMEs from 1996 to December 2004. Histograms of the mass, kinetic and potential energy of 6,335 CMEs are shown in Figure 6 and lead to several interesting observations: (i) There appears to be an upper bound of a few $\times 10^{16}$ g to the mass of a CME, (ii) about 3% of the CMEs are $< 5 \times 10^{13}$ g, (iii) the maximum kinetic energy of a CME is $10^{32} - 10^{33}$ erg, (iv) the "average CME" has mass of 1.4×10^{15} g and kinetic energy of 2.6×10^{30} erg. We compare the LASCO statistics to the data set from the Solwind instrument (Howard *et al.*, 1985) in Table I.

The difference between the two samples probably results from the larger number of small events in the LASCO database that results from the higher sensitivity, wider field of view and almost 100% coverage of LASCO compared with SOLWIND and SMM. A redefinition of the term "CME" is needed in order to distinguish "real" CMEs from small scale jets or fluctuations of the solar wind.

The total mass ejected in CMEs ranges from a few times 10^{13} g to more than 10^{16} g. Accordingly, the kinetic energy of CMEs with angular width $<120°$ ranges

TABLE I

Average CME Properties.

Parameter	LASCO	Solwind
Observing duty cycle	81.7%	66.5%
$\langle E_{\mathrm{kin}} \rangle$ (erg)	2.6×10^{30}	3.5×10^{30}
$\langle \mathrm{Mass} \rangle$ (g)	1.4×10^{15}	4.1×10^{15}
Mass flux (g/day)	2.7×10^{15}	7.5×10^{15}

from $\sim 10^{27}$ erg to $\sim 10^{32}$ erg, with an average value of 5×10^{29} erg. Some very fast and wide CMEs can have kinetic energies exceeding 10^{33} erg, generally originating from large active regions and accompanied by powerful flares (Gopalswamy *et al.*, 2005a).

3.1.2. *CME Rate*

During solar minimum, the CME rate is typically 0.5/day. The rate during solar maxima is an order of magnitude higher. Figure 7 shows that the CME rate averaged over the Carrington rotation period (27.3 days) increased from less than 1 per day to more than 5 per day. The large spikes are due to active regions that are very active producers of CMEs. The correlation between the daily CME rate and sunspot number (SSN) is less than perfect, especially for large SSN (near solar maximum). CMEs occur around solar maximum with a relatively high rate from the polar crown filaments (PCFs), but have nothing to do with sunspots; hence, they need not be correlated with SSN. Both SSN and CME rates show a double maximum (late
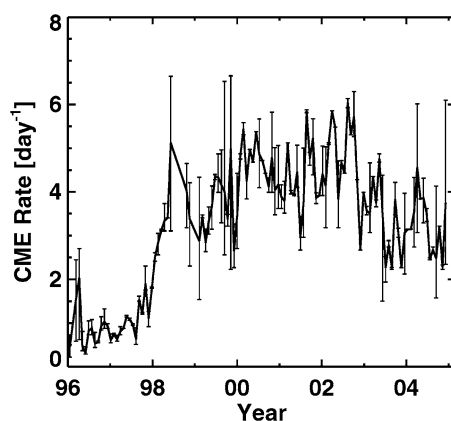

Figure 7. CME rate over the course of the SOHO mission from the LASCO CME catalog (Yashiro *et al.*, 2004).

2000 and early 2002). The low-latitude (LL) CME rate is generally higher than the high-latitude (HL) rate, but occasionally they can be very close. The cessation of HL CMEs coincided with the polarity reversal at the solar poles (Gopalswamy *et al.*, 2003b). The HL CMEs provide a natural explanation for the disappearance of PCFs, which need to be removed before the poles can acquire the open field structure of the opposite polarity.

3.1.3. *Variability of CME Speed*

The speed of a CME is usually measured by constructing a time-height diagram for the fastest moving feature of the CME front as it appears projected on the plane of the sky (POS). Inevitably, the POS values can deviate from the real radial speed of the CME front, depending on the actual direction of the motion. That may explain in part why different observers reached different conclusions. In the study by Howard *et al.* (1985) the mean POS speed of CMEs was found to increase with increasing solar activity. However, SMM data did not show a significant difference in the average speed of CMEs between solar activity minimum and maximum (Hundhausen, 1993). SOHO data confirmed an increase (Gopalswamy, 2004) as demonstrated in Figure 8. The annual mean speed increased from slightly below 300 km/s in 1996 to about 500 km/s in 2000. The speed showed a dip in 2001, as did the CME rate, and continued to increase to the second maximum in 2002. However, the speed did not decline after the 2002 maximum, but peaked in 2003. This is mainly because of the exceptional active regions (10484, 10486, and 10488) that produced fast and wide CMEs during October–November 2003. The speeds then started to decline with the CME rate.

These results must be taken with some caution. It is unclear at what distance the speed determinations were performed. Note that all histograms show CME speeds of less than 200 km/s, i.e. less than the minimum speed of even the slowest solar wind. That indicates that some of the CME speeds were determined close to the
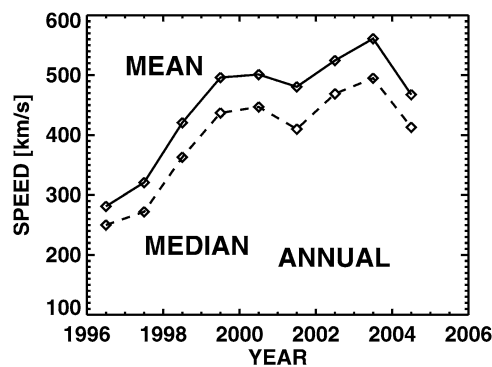

Figure 8. CME speeds over the course of the SOHO mission from the LASCO CME catalog (Yashiro *et al.*, 2004).

limb where CMEs are still being accelerated. The CME catalog maintained by Yashiro *et al.* (2004) shows how dramatically different the acceleration profiles for CMEs can be out to about 10 $R_\odot$. In order to quantify this huge diversity one has to make sure that the quantities under investigation (speed, width, latitude, mass) are all measured at the same "safe" distance from the Sun where they have reached constant speed, at about 15 $R_\odot$. Another reason for considering these results with some skepticism is the projection effect mentioned above. Burkepile *et al.* (2004) analyzed the role of these projection effects very carefully and based their study on 111 "limb" events observed by SMM. They found that these CMEs that are not affected by projection effects have a substantially higher average speed (519 ± 46 km/s) than that obtained from all SMM CMEs.

3.1.4. *CME Latitudes*

The latitude distribution of CME sources depends on how closed field regions are distributed on the solar surface. During the rising phase of cycle 23 (1997–1998), the CME latitudes were generally close to the equator and subsequently spread to all latitudes. During the maximum phase, there are many polar CMEs, and the number of such CMEs was larger in the southern hemisphere and occurred over a longer time period than in the north. This variation of CME latitude over the course of the solar activity cycle is consistent with previous measurements from Skylab/ATM (Munro *et al.*, 1979), P78-1/Solwind (Howard *et al.*, 1985) and SMM/CP (Hundhausen, 1993). However, Burkepile *et al.* (2004) noted the strong effect geometrical projection can have when relating CME apparent latitudes to source latitudes. They conclude that a much smaller percentage of limb CMEs were centered at high latitudes than was previously reported.

3.2. Morphological Properties

CMEs observed in white light are highly structured and are three-dimensional in nature. Many CMEs, especially the ones originating from filament regions show a three-part structure: a bright frontal structure, a dark void, and a bright core (Hundhausen, 1987). This is not seen in all CMEs. Even in prominence related CMEs, the three-part appearance depends on the location of the underlying prominence (Cremades and Bothmer, 2004). If the CME is super-Alfvénic, it can be expected to drive a shock ahead of it. Some CMEs have been interpreted as flux ropes (Chen *et al.*, 2000; Plunkett *et al.*, 2000). Some CMEs have voids with no prominence in them. Jets and narrow CMEs with no resemblance to the three-part structure have also been observed (Howard *et al.*, 1985; Gilbert *et al.*, 2001; Wang and Sheeley, 2002b; Yashiro *et al.*, 2003).

CMEs occurring close to the disk center often appear to surround the occulting disk of the coronagraph and are known as halo CMEs (Howard *et al.*, 1982). Only ~3% of the SOHO CMEs are halos, but about 11% have a width exceeding 120°. CMEs with apparent widths between 120° and 360° are known as partial halos.

Halos can be "front-sided" or "back-sided," and for differentiation simultaneous disk observations are required. Some halos are asymmetric, heading predominantly above one limb with weak extensions on the opposite limb. These CMEs generally originate from locations closer to the limb than to disk center. The average speed of halo CMEs is 1000 km/s, more than 2 times the average speed of all CMEs (see Figure 5). This is clearly a result of bias. Halo CMEs are like ordinary CMEs that occur near disk center, but only the most powerful are detectable. (Yashiro *et al.*, 2004; Tripathi *et al.*, 2004). When front-sided, these "halo" CMEs can directly impact Earth causing geomagnetic storms, provided the magnetic field contained in the CMEs has a southward component (e.g. Gonzalez and Tsurutani, 1987).

The cone angles of CME expansion and, more generally, the shapes of the expanding CMEs are usually well maintained (Plunkett *et al.*, 1998). The CME shapes remain "self-similar." In other words, the ratio between lateral expansion and radial propagation appears to be constant for most CMEs. Low (1982) had already noticed the "often observed coherence of the large-scale structure of the moving transient," which could be explained by what he called "self-similar evolution." He studied the expulsion of a CME quantitatively on the basis of an ideal, polytropic, hydromagnetic description and found self-similar solutions that describe the main flows of white light CMEs as they are observed (see also Low, 1982, 1984, 2001; Gibson and Low, 1998).

The shapes of the vast majority of CMEs appear to be consistent with a nearly perfect circular cross section (Cremades and Bothmer, 2005). Indeed, halo CMEs moving exactly along the Sun-Earth line exhibit generally a circular and smooth shape. This observation is rather surprising in that CMEs are usually associated with the eruption of 2D elongated filament structures. Therefore, CMEs can be described in terms of "cone models" (for further discussion see the review by Schwenn (1986) and Cremades and Bothmer (2004). Thus the apparent lateral CME expansion speed can be considered independent of the viewing direction, and it is the only parameter that can be uniquely measured for any CME, be it on the limb or pointed along the Sun-Earth line, on the front or back side.

Schwenn *et al.* (2005) selected a representative subset of 57 limb CMEs and determined both the radial speed, V_{rad}, of the fastest feature projected onto the plane of the sky, and the expansion speed, V_{exp}, measured across the full CME in the direction perpendicular to V_{rad}. They found a striking correlation between the two quantities, $V_{rad} = 0.88 V_{exp}$, with a correlation coefficient of 0.86. This correlation holds for the slow CMEs as well as the fast ones, for the narrow ones as well as the wide ones. This means that the quantity V_{exp}, which is always uniquely measurable for all types of CMEs, even halo and partial halo CMEs, can be used as a proxy for the radial propagation speed V_{rad} that is most often not accessible. Schwenn *et al.* (2005) established the lateral expansion speed V_{exp} as a pretty accurate though empirical tool for predicting the travel time of ICMEs to Earth.

There have been attempts to reveal the true 3D topology and internal structure of CMEs. Crifo *et al.* (1983) found the structure of a particular CME to be a 3D

bubble rather than a 2D loop. Moran and Davila (2004) analyzed polarized images from LASCO. Their reconstruction of 2 halo CMEs suggests that these events were expanding loop arcades. Polarized measurements can indeed play a significant role for understanding CME structure and need to be pursued in the future, as Dere *et al.* (2005) stated. 3D structure can also be deduced by using Doppler shift to obtain line-of-sight velocities. This technique has been used to investigate the helical structure of a CME (Ciaravella *et al.*, 2000), the structure of the CME leading edge (Ciaravella *et al.*, 2003) and the relationship between a CME bubble and the hot plasma within it (Lee *et al.*, 2006).

3.3. PHYSICAL PROPERTIES

White-light coronagraphs detect electrons irrespective of the temperature, so spectral observations are needed to infer densities and temperatures, and radio observations provide density and magnetic field information.

3.3.1. *Density*

White-light images provide electron column densities integrated along the line of sight in different parts of the CME. For the scattering characteristics of the electrons it is generally assumed that they are in the plane of the sky, giving a lower limit to the mass (Vourlidas *et al.*, 2000). The white-light densities vary among events but they are generally of the order of 10^4–10^5 cm^{-3} for middle corona heights (4–7 $R_\odot$). They represent significant enhancements over the background corona ($\sim$10–100 times below 6 $R_\odot$ falling to $\sim$3–4 times at 30 $R_\odot$).

Radio observations of thermal emission provide density diagnostics of the prominence, the cavity and the leading edge. Multiwavelength observations of erupting prominences constrain their densities and temperatures (Irimajiri *et al.*, 1995). These estimates depend strongly on the surface filling factor assigned to the cool threads and the scale length of the filament. Akmal *et al.* (2001) found densities above 7×10^8 cm^{-3} at 1.3 $R_\odot$ for optically thick CME plasma at 10^4 K. At decimetric wavelengths, filaments are seen also as depressions on the disk (Marqué, 2004) corresponding to a low density structure surrounding the filament (a cavity), as also seen in white-light and X-ray (Hudson *et al.*, 1999) observations. The measurements taken with the Nançay radioheliograph are compatible with electron density depletions between 25 and 50% of the mean coronal density (75% for some filaments). CME leading edges observed at meter wavelengths require subtraction of quiet Sun emission (Bastian and Gary, 1997; Gopalswamy and Kundu, 1992; Kathiravan *et al.*, 2002). The densities inferred from these observations are of the order of those obtained from white-light coronagraphic observations.

Ultraviolet spectra provide two different types of density measurements. Classical density-sensitive line ratios of O IV lines (Wiik *et al.*, 1997) and OV lines (Akmal *et al.*, 2001) have been measured in a few events. At 3.5 $R_\odot$, Akmal *et al.* find densities from 1.4×10^6 cm^{-3} to more than 10^8 cm^{-3}. Both measurements

pertain to fairly cool CME core material. The density can also be determined from the ratio of the collisionally and radiatively excited components of a UV spectral line. This method can be used at speeds below about 100 km/s, where a line is pumped by the emission in the same line from the solar disk, or at speeds near 369 and 172 km/s, where O VI $\lambda 1037$ is pumped by C II $\lambda\lambda 1036.3$, 1037.0 (e.g., Dobrzycka *et al.*, 2003). It can also be used at speeds near 1755 and 1925 km/s, where OVI $\lambda 1032$ is pumped by Lyβ, and O VI $\lambda 1037$ is pumped by O VI $\lambda 1032$ (Raymond and Ciaravella, 2004). The latter study found densities ranging from 1.3×10^6 to 4×10^7 cm^{-3} at 3 $R_\odot$.

3.3.2. *Temperature*

YOHKOH images show gas at several million K electron temperatures. EIT and TRACE images are often interpreted under the assumption that the 195 Å image shows Fe XII emission formed at 1.5×10^6 K, though O V (2×10^5 K) or Fe XXIV (2×10^7 K) can contribute. It is often possible to discriminate between Fe XII and Fe XXIV on morphological grounds, however.

Spectra can constrain the CME temperature in several ways. The measured line widths give upper limits to the ion kinetic temperatures, and electron temperatures can sometimes be obtained from the ratio of two lines of a single ion if their excitation potentials differ (e.g. Ciaravella *et al.*, 2000). Lower limits on electron temperature can also be inferred from collisionally excited lines if the density and column density are known.

3.3.3. *Elemental Composition and Ionization State*

The composition of CME material is basically that of the pre-CME prominence or coronal plasma, though the charge state may be altered. Ciaravella *et al.* (1997) found a weak FIP (First Ionization Potential) enhancement, consistent with prominence abundances in cool CME core material. Structures identified as post-CME current sheets have been observed in a few cases, and the elemental composition matches that of the nearly active region (Ciaravella *et al.*, 2002).

Simply detecting a spectral line reveals the presence of that particular ionization state, and species from H I and C II to [Fe XVIII] and [Fe XXI] have been detected in various CMEs (e.g. Innes *et al.*, 2001; Raymond *et al.*, 2003). The faster, more powerful CMEs show little cool plasma, but the high temperature ions [Fe XVIII], [Fe XX] and [Fe XXI] are present (Raymond *et al.*, 2003; Innes *et al.*, 2001; 2003a,b).

The charge state of CME plasma is frozen in below 2 $R_\odot$ for typical CME speeds and densities. Cool prominence material often appears in absorption against background coronal emission in EIT images, indicating neutral gas. As it rises it often becomes bright in the 195 Å band, indicating emission in either O V or Fe XII (e.g. Ciaravella *et al.*, 2000; Filippov and Koutchmy, 2002).

3.3.4. *Magnetic Field*

At radio wavelengths, the analysis of gyroresonance emission, of polarization spectra of the thermal emission, of microwave QT-propagation (Quasi-Transverse), and of gyrosynchrotron emission, provides different techniques used to measure coronal magnetic fields in prominences, coronal holes, loops and CMEs (Gary and Keller, 2004). Radio observations indicate a magnetic field strength of 1 G in the corona at a heliocentric distance of 1.5 $R_\odot$ (see, e.g., Dulk and McLean, 1978). The field strength is 3–30 G in quiescent prominences and 20–70 G in active prominences (see e.g., Tandberg-Hanssen, 1995). The magnetic field in the cavity is virtually unknown, but a higher field strength may be required to compensate for the lower density.

3.4. ASSOCIATED PHENOMENA

Eruptive prominences (EPs) observed in Hα or microwaves frequently accompany CMEs (Hundhausen, 1993; Hanaoka *et al.*, 1994; Gopalswamy *et al.*, 1996). They represent a good proxy for the configuration of the coronal magnetic field; they overlie polarity inversion lines, and the surrounding coronal magnetic fields are highly sheared. CMEs accompanied by an EP are particularly interesting to study in order to predict their magnetic topology (Rust and Kumar, 1994; Martin and McAllister, 1996; Bothmer and Schwenn, 1996; Rust, 2001).

Flares and CMEs may or may not be related to each other (Harrison, 1986, 2003), although when a CME does occur it usually has a close flare association. A strong X-ray flare can occur in the absence of CME and conversely a CME is not necessarily associated with a flare. However, when both flares and CMEs are produced conjointly, it seems that they share at their onset the same energetic processes for CME acceleration and flare energy release (Zhang *et al.*, 2004).

Long Duration Events (LDEs) observed at soft X-ray wavelengths are closely associated with CMEs (Sheeley *et al.*, 1983; Webb and Hundhausen, 1987). LDEs are observed as the appearance of large-scale loop systems, also called eruptive arcades (EAs) or post-eruptive arcades (PEAs), which often form and evolve in the aftermath of coronal eruptions. Their detection depends on their temperature, therefore on the wavelength in which observations are made. They are observed to occur in the lower corona close to the onset site of the eruption (Figure 9), which illustrates the bright loops of the Bastille Day flare). PEAs observed at 195 Å by EIT have almost one-to-one correlation with CMEs (Tripathi *et al.*, 2004).

Halo CMEs can be associated with many other manifestations seen on the solar disk. They are associated with EUV and soft X-ray dimmings, disappearing trans-equatorial loops, Hα Moreton waves and EIT waves (Pick *et al.*, 2006, this volume). It seems that for most of the large flare/CME events, all these manifestations are
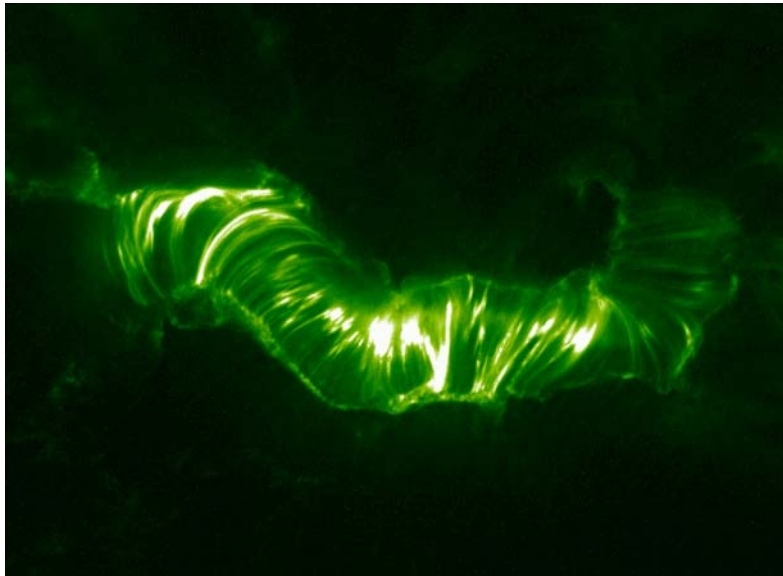
Figure 9. TRACE 195 Å image of the flare arcade during the Bastille Day event on July 14, 2000.

present. One interesting observational signature of CMEs on the solar disk is the evolution from a sheared structure to arcade structure (Sakurai *et al*., 1992). The pre-eruptive scenario is often marked by the presence of an "S-shaped" sigmoid structure which denotes the dominant helicity in that hemisphere (Gopalswamy *et al*., 2006, this volume).

Another important signature of an on-disk CME is the observation of transient dimming observed in X-rays and EUV (e.g., Hudson *et al*., 1996; Gopalswamy *et al*., 1997; Pick *et al*., 2006, this volume). These dimmings have been interpreted as the opening of the initially closed field lines during the initial phase of a CME indicating mass loss of the order of 10^{14} g, an order of magnitude smaller than in a typical CME. Front-side halo events may start with the disappearance of trans-equatorial loops (TELs) observed in X-rays (Khan and Hudson, 2000; Pohjolainen *et al.*, 2001).

Radio bursts are produced by plasma emission processes when accelerated electrons travel along open field lines or loop systems. The U and J bursts exhibit a turn-over frequency at the top of the loop. Different components of type IV bursts are associated with different parts of the CMEs. Bastian *et al.* (2001) imaged CME loops, called radio CMEs, extending to about 3 $R_\odot$, behind the CME front (Figure 10). These radio emitting loops are the result of nonthermal synchrotron emission from 0.5–5 MeV electrons interacting with magnetic fields of about 0.1 to a few Gauss. Pick *et al.* (2006, this volume) discuss the relationships of coronal shocks to radio measurements in more detail.
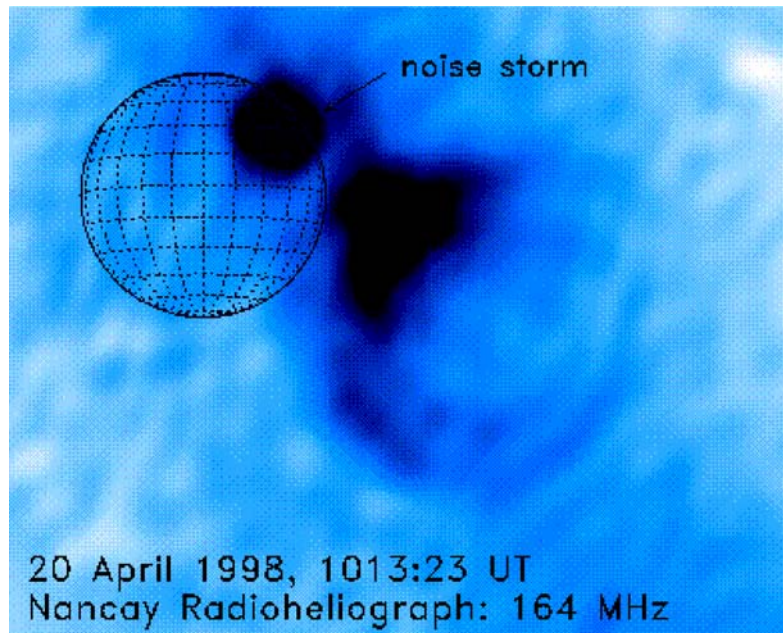
Figure 10. Snapshot of the radio CME observed on 20 April 1998 at 164 MHz at the time of maximum. The background emission from the Sun has been subtracted. Radio emission from a noise storm is present to the northwest. The brightness of the CME is saturated in the low corona because the map has been clipped at a level corresponding to a brightness temperature $T_b = 2.6 \times 10^5$ K. The radio CME is visible as a complex ensemble of loops extending to the southwest. (From Bastian *et al*., (2001)).

4. CME Evolution and Dynamics

4.1. KINEMATIC EVOLUTION OF CMES

A CME is basically a moving feature and, therefore, a key aspect of CME study is the kinematic evolution of a CME through the corona. One of the most interesting observational questions is when and where a CME gets accelerated in the corona. Both propelling and retarding forces acting on a CME need to be considered.

CMEs usually travel at a relatively constant speed with minor acceleration or deceleration. The statistical distribution of CME accelerations in the LASCO C2/C3 field of view shows a peak value close to zero and for a majority of events the acceleration within only ± 20 m/s^2 (Moon, 2002; Yashiro *et al*., 2004). While the slowest CMEs tend to show positive acceleration, the fastest CMEs decelerate in the outer corona (Gopalswamy *et al*., 2000a). This indicates that the major acceleration of a fast CME mainly occurs in the inner corona, i.e. below $2\,R_\odot$ and the subsequent evolution is primarily controlled by the interaction between the CME and the medium through which it propagates.

The complete kinematic evolution of a number of CMEs has been well observed by combining LASCO C1 with C2/C3 observations and the SOHO/EIT observations (Srivastava *et al.*, 1999; Gopalswamy and Thomson, 2000; Zhang *et al.*, 2001). One example is shown in Figure 11, where the kinematic evolution is represented by plots of height, velocity and acceleration against time. for the June 11, 1998 event. Based on a combined study of this and some other events, Zhang *et al.* (2001) described the kinematic evolution of a CME in terms of a three-phase scenario: (1) the initiation phase, (2) the impulsive (major) acceleration phase and (3) the propagation phase. The initiation phase is characterized by a slow ascension of certain coronal features (e.g, active region envelopes, filaments) for a period of up to tens of minutes, with a speed typically below tens of km/s. The major acceleration phase is characterized by fast acceleration (e.g, from a few hundred to a few thousand m/s^2). This phase lasts typically from a few minutes to tens of minutes (it can be even longer for certain events) in which the coronal features travel a distance ranging from a fraction of a solar radius to several solar radii. After the completion of the acceleration phase, a CME appears to be fully developed and travels at a more or less constant speed, a constant angular width and a constant position angle. This phase is therefore simply called the propagation phase, when the ICME is primarily subject to drag forces (see Forbes *et al.*, 2006, this volume).

Not all CMEs necessarily display a full three-phase evolution. Events which show persistently weak acceleration (i.e., <25 m/s^2) throughout the inner and the outer corona are known as gradual or balloon-type events (Srivastava *et al.*, 1999, 2000). These CMEs are usually slower than 100 km/s in the inner corona (i.e. below 2 $R_\odot$) and eventually reach terminal speeds no higher than 400–600 km/s in the LASCO /C3 field of view. Figure 12 clearly shows the difference in the kinematic evolution of the gradual events. The speed profiles of these "balloon-type" CMEs are very similar to the slow solar wind speed profiles that Sheeley *et al.* (1997) derived by tracing small density blobs floating along like "leaves in the wind." Similarly, the "balloon-type" CMEs appear to float along and follow the slow wind's acceleration. The CME acceleration values can differ by up to a factor of 1000, as Figures 11 and 12 demonstrate. Some authors take this as evidence for different types of CMEs driven by radically different release and acceleration mechanisms (e.g., Sheeley *et al.*, 1999).

4.2. WHITE-LIGHT AND UV SIGNATURES OF SHOCK WAVES

Many CMEs propagate with speeds >1000 km/s, much larger than the characteristic sound and Alfvén speed in the solar wind. Therefore, the ejected plasma clouds should drive shocks ahead of themselves. There is plenty of indirect evidence for waves associated with CMEs (Sheeley *et al.*, 2000), but there have been only two published detections of white light shocks (Sime and Hundhausen, 1987; Vourlidas *et al.*, 2003). This does not mean that CME shocks do not have a white-light
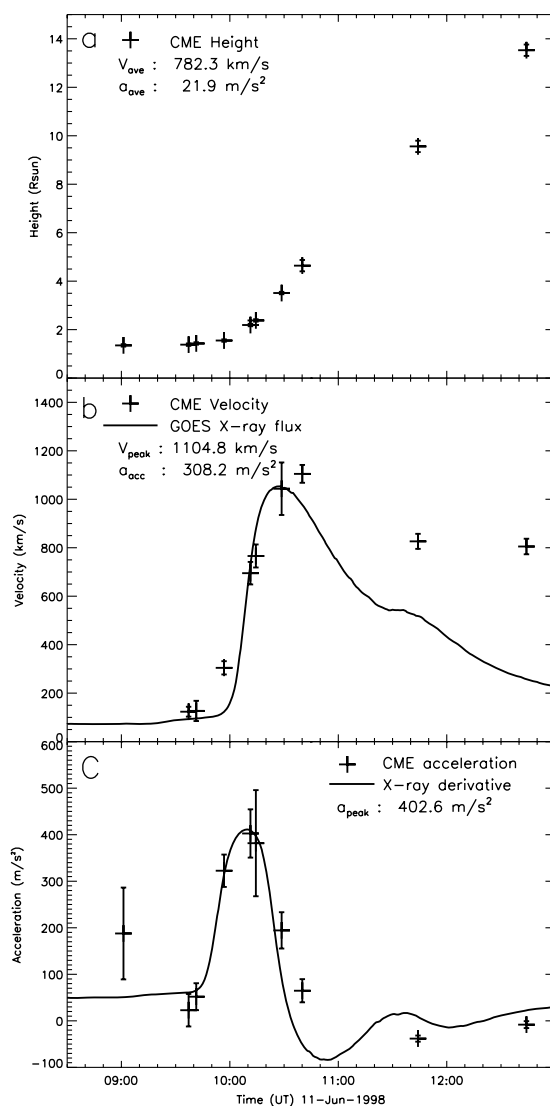
Figure 11. CME kinematic plots versus flare flux plots for the 1998 June 11 event. The three panels, from top to bottom, show CME height-time plot, velocity-time plot and acceleration-time plot (discrete plus signs with error bars), respectively. The solid curve in panel b shows the soft X-ray flux profile of the flare, which apparently correlates with the CME velocity profile during the rise phase. The solid curve in panel c shows the derivative profile of the soft X-ray flux (equivalent to the hard X-ray profile according to the Neupert effect), which apparently correlates with the CME acceleration profile in the impulsive phase. (Adapted from Zhang *et al.* (2004)).
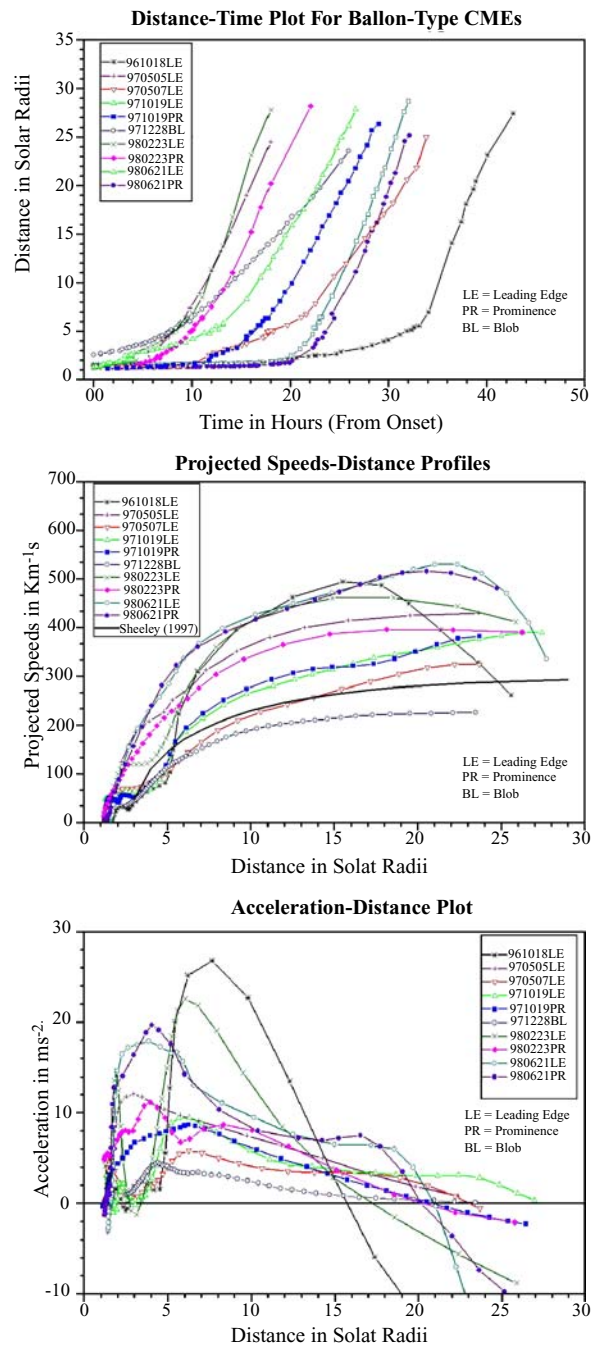
Distance-Time Plot For Ballon-Type CMEs

Projected Speeds-Distance Profiles

Acceleration-Distance Plot

Figure 12. Kinematic plots for 7 balloon-type CMEs observed by LASCO. The three panels from top to bottom show CME height-time plots, velocity-time plots and acceleration-time plots, respectively. The solid curve in the middle panel shows the speed profile as derived from "leaves in the wind" by Sheeley *et al.* (1997), adapted from Srivastava *et al.* (1999).
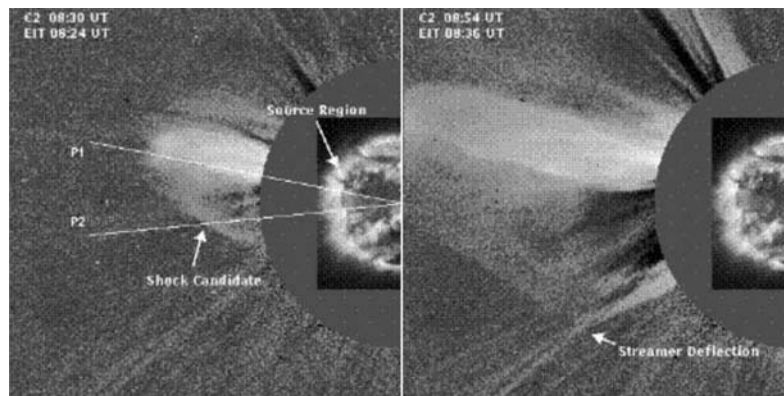
Figure 13. CME shock identification for the April 2, 1999 event. These are LASCO/C2 calibrated excess mass images. The EIT 195 image is also shown. Note the clear streamer deflection as the shock impinges on it. Adapted from Vourlidas *et al.* (2003).

signature. Rather, it is difficult to prove that a given sharp feature is indeed a shock front and not just a coronal loop or a wave front. Parker (1961, 1963) developed analytic models of interplanetary shock waves (see also Hundhausen, 1985) and interpreted one of the solutions as a compressed shell of fluid driven into the ambient medium, Simon and Axford (1966) showed that there is a second shock front that moves inwards with respect to the fluid. The complete solution consists of a shell bounded by an external shock that accelerates and compresses the ambient material and an internal shock that decelerates and compresses the fast solar wind.

Vourlidas *et al.* (2003) simulated a specific event with a detailed MHD model to show that the CME flank was actually a shock (Figure 13). Furthermore, a streamer was seen to bend as the flank impinged on it, thus providing compelling evidence that streamer deflections are indeed due to CME shocks. Although it is impractical to model every possible CME candidate to show that the front (or flank) is a shock, we know that many events exhibit similar overall morphology. Therefore, we can use the experience gained from modeling a single event and common sense to look for similar features in other events. As MHD models evolve and we understand better the white light CME morphology, we expect that the shock identification in coronagraph images may become more routine in the near future.

Shock waves are detectable in UV spectra of the corona through the high velocities, heating and compression that they produce. The shocks tend to be faint, however, and coronagraphic observations are required. UVCS has detected about 10 CME shocks so far (Raymond *et al.*, 2000; Mancuso *et al.*, 2002; Raouafi *et al.*, 2004; Ciaravella *et al.*, 2005, 2006). The most easily detectable signature is a sudden broadening of the O VI lines to a width comparable to the shock speed. Collisionally excited lines such as Si XII $\lambda52.1$ nm brighten because of the compression, while radiatively excited lines such as Lyα fade because of Doppler dimming at

(a) 1998 May 7   (b) 2001 Feb 1   (c) 1999 Dec 28   (d) 2001 Jun 4
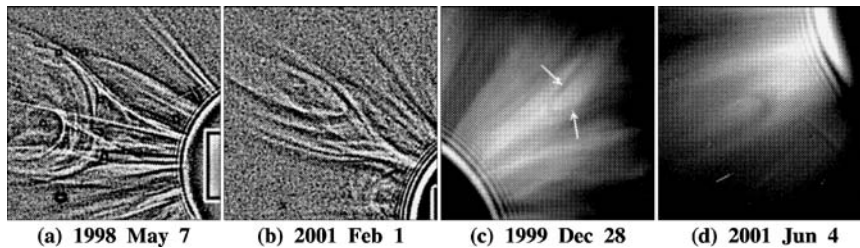
Figure 14. Examples of concave-outward structures observed with the LASCO C2 coronagraph during CME events. (a) CME with topology suggestive of a cylindrical or toroidal flux rope (edge-enhanced image). (b), (c), and (d) show dark U-shaped features. The U-loops in the December 28 and June 4 events are entrained in core material that is falling back toward the Sun (From Wang and Sheeley (2002a)).

high speeds. The UV spectra provide unique information about the heating of individual ion species and electrons in the collisionless coronal shocks. Spectra of the pre-CME corona provide the initial density, temperature and composition of the plasma, all necessary inputs for models of SEP production. More detail is given in the Working Group F chapter.

Another signature of coronal shocks is a hectometric-kilometric type II radio burst. This emission at the local plasma frequency and its harmonic is caused by energetic electrons accelerated at the shock front. The radio frequency is a direct measure of the density near the shock, and the drift rate provides a rough estimate of the shock speed. More detail is given in the paper by Pick *et al.* (2006, this volume).

4.3. EVIDENCE FOR MAGNETIC DISCONNECTION

During CME events, large-scale structures having a concave-outward topology are often observed in the white-light corona; examples are shown in Figure 14. Such structures are sometimes interpreted as evidence for magnetic disconnection (see, e.g., Illing and Hundhausen, 1983). In the majority of cases, however, we may be seeing three-dimensional flux ropes with their ends still anchored in the Sun rather than completely detached "U-loops" (Wang and Sheeley, 2002a). The *SOHO*/LASCO coronagraph has also recorded many events suggestive of ongoing disconnection, where an elongated streamer structure appears to split apart (Figure 14) or where a loop-shaped ejection with a hollow center separates into an outward- and an inward-moving component (Figure 15b). Again, the ejected component in such events is not necessarily completely detached but may represent a flux rope still connected at its far ends to the Sun. Even more frequently encountered are the multitude of small-scale inflows, in the form of dark collapsing loops and cusps, sinking columns of streamer material, and dark tadpole-shaped features
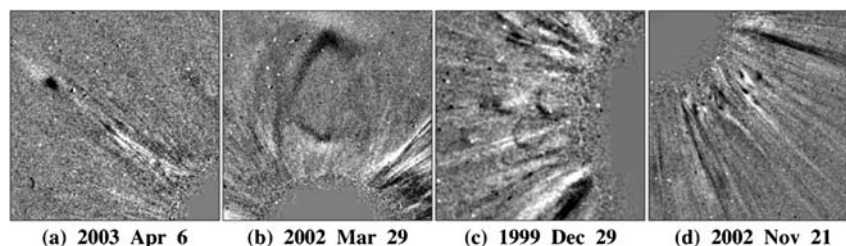
Figure 15. White-light coronagraph observations that suggest ongoing magnetic disconnection. Each panel represents the difference between two LASCO C2 images taken 20–30 min apart; white (black) means that the local coronal density has increased (decreased) during the elapsed interval. (a) Streamer detachment. (b) Looplike ejection with infalling counterpart (face-on view of a "streamer detachment"?) (c) Collapsing loops. (d) Collapsing cusps (sinking column inflows). (From Wang *et al.* (1999)).
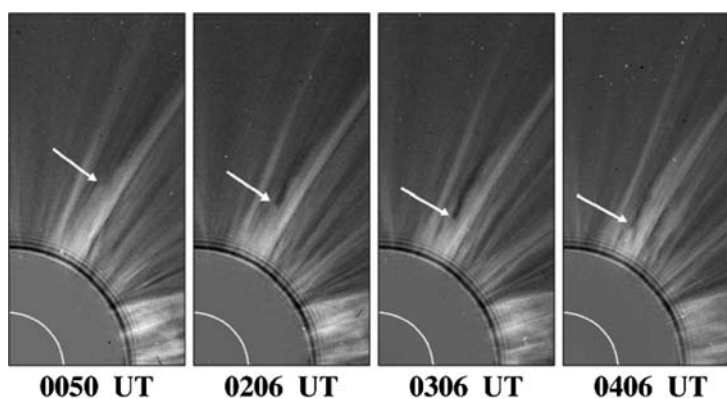

Figure 16. Inflow observed with the LASCO C2 coronagraph on October 25, 1999. The sinking column of streamer material leaves a dark depletion trail in its wake and takes on a cusp-like appearance below $r \sim 2.5 R_\odot$ (From Sheeley and Wang (2002)).

Figures 15c, d, and 16. These events, which tend to occur well in the aftermath of CMEs (and are not always associated with them), are observed only at heliocentric distances below about $5R_\odot$. Although the inflows are highly suggestive of the pinching-off of open field lines at the heliospheric current sheet, no outgoing counterparts are detected, perhaps because they are below the sensitivity threshold of the LASCO coronagraph in the region beyond $5R_\odot$.

4.4. POST-FLARE INFLOWS

Analogous inflow events have also been detected at much lower heights with *Yohkoh* soft X-ray observations, above post-flare loop systems that exhibited fan-like structures extending above the loop tops (McKenzie and Hudson, 1999). These inflows

(McKenzie, 2000) had the appearance of voids and, although moving faster than the LASCO inflows, still had speeds well below the inferred Alfvén speeds in the structures. *SUMER* confirmed these characteristics of the inflows spectroscopically (Innes *et al.*, 2003a), and the higher-resolution *TRACE* imaging showed sinuous motions as the voids appeared to slide down between the spike structures (Gallagher *et al.*, 2002). In contrast to the inflows observed by SXT, TRACE and SUMER and interpreted as plasma voids, Tripathi *et al.* (2006) discovered a bright coronal inflow observed by EIT above post-eruptive arcades after a CME eruption. This inflow provides another evidence of post-CME reconnection. Asai *et al.* (2004) found examples of such flows even in the impulsive phase of a major flare, increasing the likelihood that this phenomenon – ill-understood theoretically at present – has a direct relationship with magnetic reconnection and flare energy release.

4.5. MASS REPLENISHMENT, POST-CME RECOVERY

The observation of "transient coronal holes" using Skylab data (the term was introduced by Rust, 1983) provided the suggestion of an X-ray identification for the source regions of CME mass. This followed earlier white-light observations of "coronal depletions," which presumably showed the same phenomena in limb observations. In this picture, the post-CME recovery would appear in the low corona as the disappearance of the newly-formed holes.

Kahler and Hudson (2001) conducted a survey of transient coronal holes observed by SXT. Movie sequences with reasonable image cadence and the ability to make difference images allowed for a deeper study of the re-formation of the corona. In the conventional 2D picture of field-line opening followed by magnetic reconnection, the transient coronal holes represent the opened field; in 3D they would represent the footpoints of a large-scale flux rope. In either case the arcade resulting from reconnection would be expected simply to fill in the holes, starting at their inner edges (the outer edges of the flare ribbons) and proceeding outwards.

In the SXT data, this simple picture was not seen. The holes form in large-scale sigmoid bends of the filament channel, thus differing morphologically from the more cylindrical arcade structure. The arcade sources do advance into the hole regions, but the holes often also shrink inwards from the outside. There is no tendency for the holes simply to brighten in place, and the durations of the dimmings suggest that the open magnetic field lines may stay open for periods longer than the arcade growth. The limit to such observations is imposed by foreground/background confusion as the Sun rotates and the perspective changes.

It seems reasonable to believe that magnetic reconnection, either on a large scale or by reconnection interchange on smaller spatial scales, could contribute to the replenishment of the lost coronal mass by providing closed flux tubes capable of trapping mass. The geometry of these processes is not so clear, especially in cases without a clear conjugate pair of transient coronal holes.

4.6. TYPE IV BURST AND RADIO EJECTA: OBSERVATIONS
OF TRAPPED ELECTRONS

Type IV bursts, first identified by Boischot (1957), are long lasting continuum radio emissions with large bandwidth associated with CMEs and flares (Stewart, 1985; Robinson, 1985; Kahler, 1992). Successive episodes in the development of type IV bursts are closely associated with different phases of CME development. Nonthermal electrons, which are accelerated at the vicinity of the flare site or by a shock wave, get trapped in moving or stationary structures and are thought to produce these various long-lasting continuum emissions.

The first stage, following the onset of the flare, corresponds to broad-band emission which extends from microwave to meter wavelengths (e. g. Kundu, 1965), and is associated with a gradual hard X-ray burst (Frost, 1974). This emission lasts between 10 min and about one hour, and can be accompanied by a moving type IV emission and rising structures with velocities up to 1000 km/sec or even more. The corresponding radio sources are complex, sometimes with two components located near the foot points and a third component near the top of the arch (e.g. Wild, 1969; Gopalswamy and Kundu, 1990). Limb observations have shown that these arches are behind the CME leading edge. Spectra of moving type IV bursts are often consistent with Razin-suppressed gyrosynchrotron emission from nonthermal electrons trapped in moving magnetic structures (e.g. Ramaty and Lingenfelter, 1967; Boischot and Clavelier, 1968; Gopalswamy and Kundu, 1989).

Bastian *et al.* (2001) reported radio thin loops behind the CME front (see Figure 10). Disk observations of halo CME events showed that radio observations image a set of ejected loops that lift as part of the CME and that EUV dimming regions are observed later in the same location as the radio emitting region (Pohjolainen *et al.*, 2001). The heated prominence material can also trap electrons and propagate as narrow ejecta (e. g. Sheridan, 1970; Riddle, 1970) or "isolated plasmoids" (e.g. Gopalswamy and Kundu, 1990).

Following this first stage, stationary type IV bursts (continuum storms) can last for several hours, shifting progressively toward lower frequencies and evolving gradually into noise storm activity associated with post-eruptive loops. Such long-lasting radio emission is the signature of suprathermal electrons in the corona, broadly associated with long-lasting soft X-ray emissions (Lantos *et al.*, 1981) and transient legs in white light (Gergely *et al.*, 1979; Kerdraon *et al.*, 1983). Kahler and Hundhausen (1992) identify type IV burst sources with newly formed streamers and suggest that the energetic electrons are produced during magnetic reconnection.

Stationary type IV bursts can occur in the absence of a flare or a gradual hard X-ray or microwave outburst. They are associated with magnetic field restructuring of the white light corona (Kerdraon *et al.*, 1983; Habbal *et al.*, 1996) and filament disappearance (e.g. Lantos *et al.*, 1981). The absence of flares in these events confirms the close association of type IV bursts with CMEs because many of these signatures imply a CME. The simplest interpretation is that moving type IV bursts

correspond to magnetic structures associated with the CME, while the stationary type IV bursts correspond to quasi-stationary post-eruption arcades. In some events, moving and stationary sources are closely coupled: Figure 17 shows a broad band continuum (type IV burst) modulated by successive packets of fast sporadic bursts which coincidence closely with hard X ray peaks (Classen *et al.*, 2003). In the example shown in this Figure, the type IV burst is formed by two sources: a fast-moving one and a quasi-stationary one. The time coincidence found between the flux peaks of these two radio sources and the underlying hard X-ray source implies a causal link: they must be fed by electrons accelerated in the same region. The observations are consistent with an erupting twisted flux rope with the formation of a current sheet behind (Pick *et al.*, 2005).
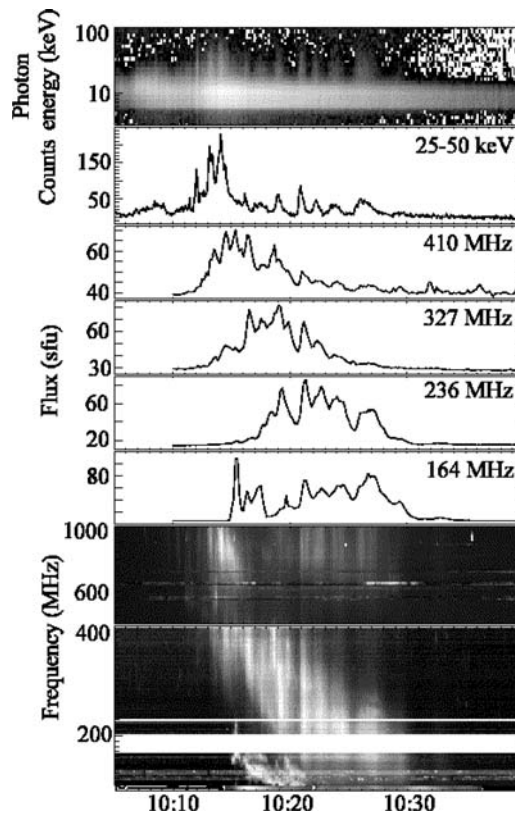

Figure 17. June 02 2002. Comparison between the photon histories measured by RHESSI (top panel), the flux evolution measured at four frequencies by the Nançay Radioheliograph, NRH, (middle four panels) and the spectral evolution measured by the Tremsdorf spectrograph, OSRA, (bottom panels). From Pick *et al.* (2005).

4.7. SIGMOIDS AND HELICITY

Active regions with pronounced soft X-ray sigmoids (S or reverse-S shaped structures; Figure 18) exhibit a greater tendency to erupt (Canfield *et al.*, 1999; Sterling *et al.*, 2000), and the eruptions produced tend to result in moderate geomagnetic storms (Leamon *et al.*, 2002). Relating the sigmoids at X-ray (and other) wavelengths to magnetic structures and current systems in the solar atmosphere is the key to understanding their relationship to CMEs. The correspondence between soft X-ray sigmoids and active region CMEs is not one-to-one. Sigmoids may also disappear and reappear without a detectable CME (see Gibson *et al.*, 2002) even while generating significant soft X-ray and EUV brightenings. Consequently, we need to understand more about the formation and evolution of sigmoid structures and explore the conditions that drive them to eruption. An important component of the physical nature of sigmoids and their relationship to CMEs is the role played by magnetic helicity.
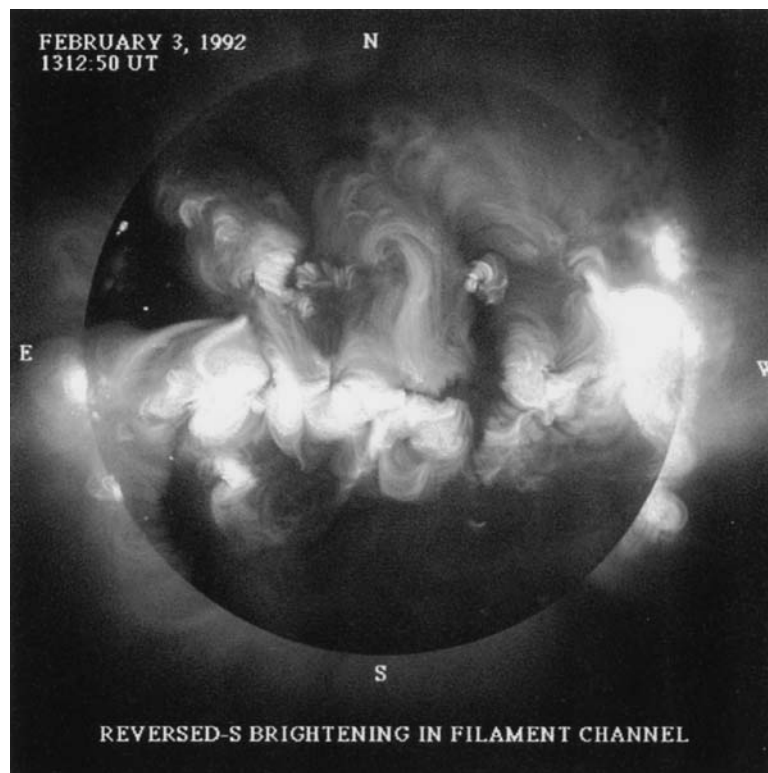

Figure 18. Yohkoh image of the X-ray corona on 1992 February 3 at 1312:50 UT. A faint, negative sigmoid brightening (center) extends across the equator.

The role of helicity injection, or "helicity-charging" (Rust and Kumar, 1994), has been a focal point in the discussion of eruptive events. In particular, it has been argued that CMEs are the means by which the solar corona expels magnetic helicity accumulated over hours and days by the combination of local shearing motions, differential rotation and the emergence of twisted flux systems (Low, 1996; DeVore, 2000; Démoulin *et al.*, 2002). The magnetic helicity is a useful quantity for studying the magnetic evolution of the CME-latent corona as it is an MHD quantity which is globally conserved on the time scales of interest (Berger, 1984).

In the solar corona, the magnetic helicity and free magnetic energy must be supplied by the photospheric or sub-photospheric activity, either in the form of the emergence of twisted structures or the in-situ shearing of previously emerged structures. Devore (2000) has argued that a significant quantity of magnetic helicity is injected by the action of differential rotation over the lifetime of an active region; enough to explain the total "ejected" helicity detected in interplanetary magnetic clouds, the interplanetary counterparts of CMEs (Gosling *et al.*, 1995). However, this assertion has been contested by Démoulin *et al.* (2002) and Green *et al.* (2002) who argue that the helicity injected by differential rotation is 5 to 50 times smaller than that inferred to be carried away in CMEs, requiring the emergence of sub-photospheric structures with significant twist as the dominant source of helicity in active regions.

In addition to the effect of differential rotation, strong local shearing may contribute significantly to the helicity injection into large but otherwise local structures associated with active regions. Recent studies by Kusano *et al.* (2002), Nindos and Zhang (2002) and Moon *et al.* (2002) have demonstrated that multiple flaring is often associated with regions of strongly sheared footpoint motions and local helicity injection. In the case discussed by Kusano *et al.* (2002) the shearing motions can contribute as much, if not more, helicity as the flux emergence.

4.8. EIT WAVES

Observations with EIT revealed a new wave phenomenon, the so-called coronal flare or EIT-waves (Moses *et al.*, 1997; Thompson *et al.*, 1998). These waves appear as bright rims sometimes circularly expanding around the flaring active region and propagating over a hemisphere of the Sun at speeds of of 200 to 300 kilometers per second. The EIT-waves are reminiscent of Moreton waves (Moreton and Ramsey, 1960; Thompson *et al.*, 1998), but they appear in EUV spectral lines emitted by a hot corona, whereas the Moreton waves are seen in Hα at velocities in the range 440–1125 km/s with mean value 650 km/s (Smith and Harvey, 1971).

The relationships among EIT waves, Moreton waves, type II radio emission and CMEs, as well as theoretical models are discussed by Pick *et al.* (2006, this volume).

4.9. INTERACTING CMES

The combination of CME data from SOHO/LASCO and radio data from the Wind/ WAVES helped identify the energetic nature of colliding CMEs within the LASCO field of view. When a fast CME overtakes a slow CME from the same solar source or a neighboring solar source, often an enhanced radio emission is detected in the radio dynamic spectrum. If such an interaction results in a single resultant CME, the process is referred to as "CME cannibalism" (Gopalswamy *et al.*, 2001, see Figure 19). Given the high rate (6 per day) of CME occurrence during solar maximum and the observed range of speeds, one would expect frequent interaction between CMEs. In the best examples, the apparent interaction seen in LASCO images coincides with a radio enhancement at the frequency corresponding to the plasma frequency at the observed distance from the Sun (e.g. Burlaga *et al.*, 2002). The mechanism of radio enhancement can be interpreted as follows: when the shock driven by the second CME passes through the high density of the first CME, it encounters a region of low Alfven speed (inversely proportional to square-root of density) and hence its Mach number increases temporarily. A high Mach number shock accelerates more electrons resulting in the enhanced radio emission. There may be other mechanisms that boost the efficiency of shock acceleration depending on the magnetic topology of the preceding CME and the turbulence in its aftermath.

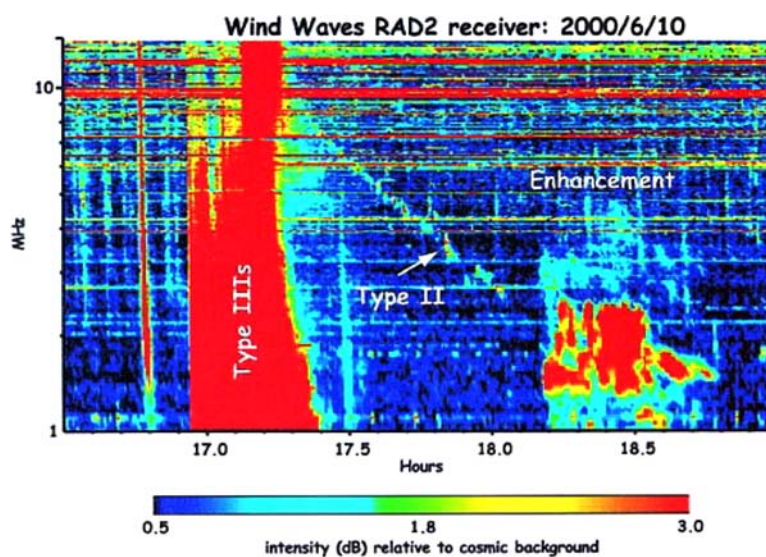*Figure 19.* Wind/WAVES dynamic spectrum in the 1–14 MHz range obtained by the RAD2 receiver. The vertical features are type III-like bursts due to electron beams escaping from the shock along open field lines. The thin slanted feature is the type II burst. The enhancement in question is the bright emission between 18:12 and 18:48 UT. It corresponds exactly to the time of interaction between two ICMEs (Gopalswamy *et al.*, 2001).

The CME interaction is also relevant for SEPs because the same shock acceler-ates electrons and ions. If the shock propagates through a preceding CME, trapping of particles in the closed loops of preceding CMEs can repeatedly return the parti-cles back to the shock, thus enhancing the efficiency of acceleration (Gopalswamy *et al.*, 2004; Kallenrode and Cliver, 2001). A systematic survey of the source re-gions of large SEP events of cycle 23 has revealed that the SEP intensity is high when a CME-driven shock propagates into a preceding CME or its aftermath origi-nating from the same solar source (Gopalswamy *et al.*, 2004, 2005). The existence of preceding CMEs can greatly enhance the turbulence upstream of the shock, re-sulting in shorter acceleration time and higher intensities for SEPs (Li and Zank, 2005). In addition, the large scatter in the CME speed – SEP intensity plots (Kahler, 2001) is significantly reduced when the interacting and non-interacting cases are considered separately. The preceding CMEs could accelerate seed particles for the following stronger shock. Presence of seed particles seems to make a difference in the resulting intensity of the SEP events (Kahler, 2001).

5. Reconnection: Observable Signatures?

Magnetic reconnection is thought to play a fundamental role in driving or at least accompanying a number of transient phenomena in the solar atmosphere, including solar flares and CMEs. The belief of the importance of magnetic reconnection comes from a combination of theoretical models and a large number of indirect signatures. We present here a summary of the observable signatures pointing to the role of reconnection in CMEs and related phenomena.

5.1. Evidence for Current Sheets

In the classical reconnection model, oppositely directed magnetic field lines get stretched out to form a current sheet defined by a diffusion region where the mag-netic field reconnects, releasing energy (e.g. Kopp and Pneumann, 1976). In most reconnection models the formation, or at least presence, of a current sheet is crucial for reconnection to occur. The standard picture for the eruption of a CME involves the reconnection of the magnetic field in a geometric configuration in which the rising CME is connected to an X-type magnetic neutral point via an extended current sheet (Figure 20). Models (Lin and Forbes, 2000; Linker *et al.*, 2001) pre-dict that an extended, long-lived current sheet must be formed for any physically plausible reconnection rate. Formation of the current sheet in such a configuration drives conversion of the free energy in the magnetic field to thermal and kinetic energy, and can cause significant observational consequences, such as growing post-flare/CME loop system in the corona and fast ejections of the plasma and the magnetic flux.
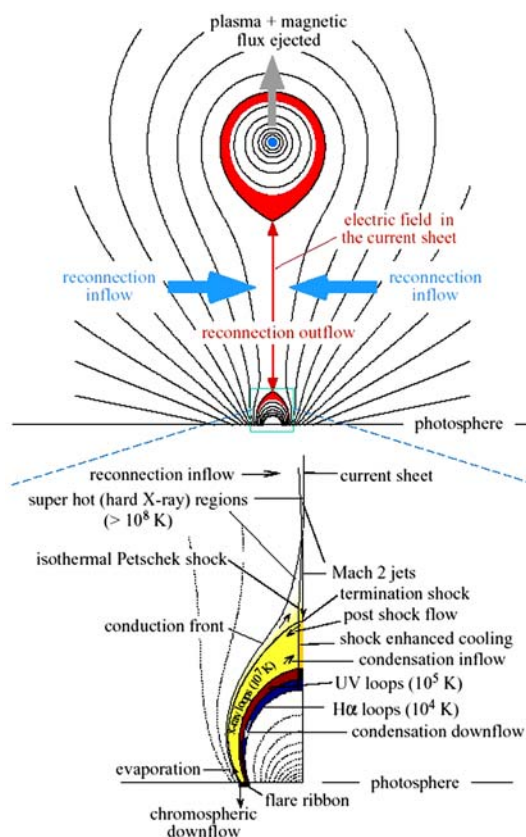
Figure 20. Schematic picture of flare loops, CME, and the current sheet between them (Lin *et al.*, 2004). *Upper part:* Sketch of the flux rope/CME model of Lin and Forbes (2000) showing the eruption of the flux rope, the current sheet formed behind it, and the postflare/CME loops below, as well as the inflows and outflows associated with the reconnection. *Lower part:* Enlarged view of the postflare/CME loops (adapted from Forbes and Acton, 1996). The upper tip of the cusp rises as reconnection happens continuously.

In order to confirm the role of reconnection in CME initiation it is therefore necessary (although not sufficient) to determine whether current sheets can be identified behind an erupting CME. Such a current sheet would be extremely thin due to the high electrical conductivity of the solar corona (see Ko *et al.*, 2003) making observation of this phenomenon difficult. On the other hand, because it is difficult to dissipate the current sheet once it forms it can exist as a well-defined structure for hours or even days (Lin, 2002); indeed, a coronal helmet streamer is normally stable. Despite many decades of indirect observations suggesting the presence of a current sheet, such as soft X-ray cusp structures (Tsuneta, 1996) and horizontal inflow (Yokoyama *et al.*, 2001) direct observations of the formation and evolution of a current sheet in the solar atmosphere have been lacking. However,

the observations from white light data discussed above sometimes do suggest the presence of large-scale current sheets in the solar corona associated with CMEs. Joint EUV (EIT), hard X-ray and radio observations of a type IV bursts also suggest magnetic reconnection in a current sheet (see Section 4, subsection on type IV emission).

Recently, a number of investigations have confirmed the presence of large-scale narrow structures behind an erupting CME suggestive of the classic current sheet topology. Sui and Holman (2003) have reported the formation of a large-scale current sheet associated with an M1.2 flare observed by RHESSI on 15 April 2002. This conclusion is based on a number of different facets observed. In particular, the RHESSI images show a dramatic change in the apparent magnetic topology suggesting a transition from an X-type to a Y-type configuration as the current sheet formed. The temperature structure of this flare suggests that a current sheet formed between a source high in the solar corona and the top of the flaring loops.

CME eruptions observed in white light and UV coronagraph data have also pointed to the existence of current sheets in the corona. Webb *et al.* (2003) show that bright rays observed in conjunction with CMEs with SMM are consistent with the existence of current sheets lasting for several hours and extending more than 5 solar radii into the outer corona. The evidence for current sheets was further strengthened by UVCS observations which exhibited a very narrow, very hot feature in the Fe XVIII line between the arcade and the CME, consistent with the eruption-driven current sheet predicted by the initiation models (Ciaravella *et al.*, 2002). Finally, Ko *et al.* (2003) analyzed an eruption which occurred on January 8, 2002 and which was observed by a LASCO, EIT and CDS on SOHO and the Mark IV K-Coronameter on Mauna Loa. They found that the properties and behavior of the observed plasma outflow and the highly ionized states of the plasma inside these streamer-like structures expected from magnetic reconnection in a current sheet (see Pick *et al.*, 2006, this volume). Figure 21 shows a reconstructed view of the April 21, 2002 CME as it would be seen from the West limb in O VI and [Fe XVIII] (Lee *et al.*, 2006). This reconstruction, based on the intensities and Doppler shifts observed by UVCS, shows a bar-like structure in the high temperature [Fe XVIII] emission (dark red), which is most easily interpreted as the part of the current sheet just below the CME core, though other interpretations cannot be excluded.

The aftermath of reconnection often includes signatures of strong heating to many millions of degrees in the solar corona. Yohkoh/SXT demonstrated that in the late phase of CME-related solar flares, high temperature soft X-ray cusp-shaped features were common (Tsuneta *et al.*, 1992) and thus this morphology points to an energy source in the solar corona suggestive of large-scale reconnection expected from many flare models.

Potentially stronger soft X-ray evidence was presented by Sterling and Hudson (1997) who found a characteristic X-ray morphology to be associated with CME formation, as detected by the formation of "transient coronal holes," a form of dimming originally identified in Skylab soft X-ray images. The sigmoid, identified
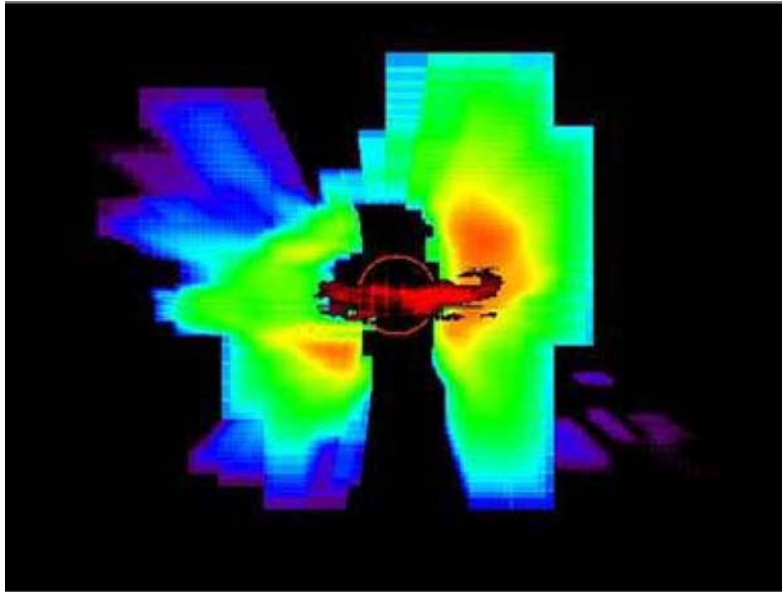
Figure 21. Image of the April 21, 2002 limb CME as it would be seen from the West limb based on a 3D reconstruction from UVCS data. The O VI emission (rainbow colors) shows the expected halo morphology, while the [Fe XVIII] emission (dark red) shows a bar-like structure which is just below the CME core when viewed from Earth or from solar north. The reconstruction uses Doppler velocities to determine the structure along the line of sight (Lee *et al.*, 2006).

with a hot component aligned with a filament channel, evolves during the event into an arcade perpendicular to it. This suggests "dipolarization" responsible for energy release following reconnection.

The cusp configuration in itself does not unequivocally imply that reconnection is ongoing. Magnetic reconnection in such a geometry also requires the presence of an inflow into the X-point (in a 2D representation). This has been surprisingly hard to detect, perhaps because the inflowing plasma is expected to be of extremely low-density being associated with open or opening field lines. Combining soft X-ray and EUV observations of a flare on the East limb of the Sun, Yokoyama *et al.* (2001) found a large-scale coronal cusp with strong evidence for an inflow of plasma into the cusp (X-point) region. Figure 22 shows a time-distance plot for the EUV emission integrated along a line passing through the observed location of the X-point. The figure clearly shows the 1 MK plasma moving inwards. Lin *et al.* (2005) show UV and visible-light evidence for both inflow and outflow in a post-CME current sheet.

An intriguing and perplexing dynamic phenomenon associated with erupting flares and CMEs has received attention in recent years. Modern soft X-ray and EUV observations frequently show a fan of spikes extending above the loop system of a flare arcade. McKenzie and Hudson (1999) found structures moving downward
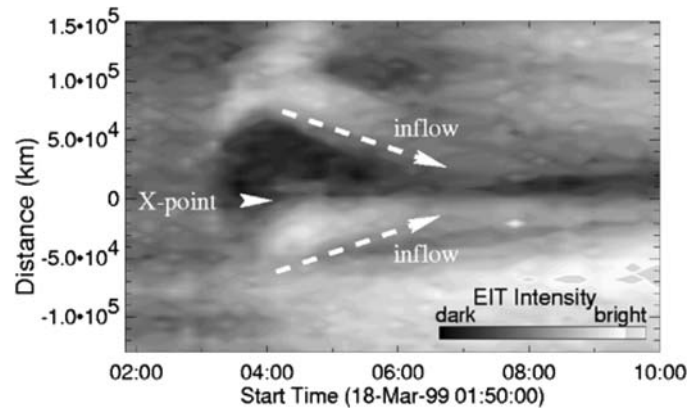
Figure 22. Time Evolution of the one-dimensional distribution of EUV intensity across the X-point, from Yokoyama *et al.* (2001).

through this fan, normally voids (Innes *et al*., 2003a), during flare evolution. These downflows are most readily seen in recent TRACE observations of the 2002 Apr 21 event (Figure 23). It is not yet clear whether these downflows in the lower corona are the same phenomenon observed in white light at much greater distances from the Sun. However, given the apparent magnetic nature of the downflow structures observed by TRACE and SUMER, the association with post-reconnection dynamics is attractive. This ready identification with the reconnection outflow jet, expected from the models is problematic, however, because the speeds observed (up to a few
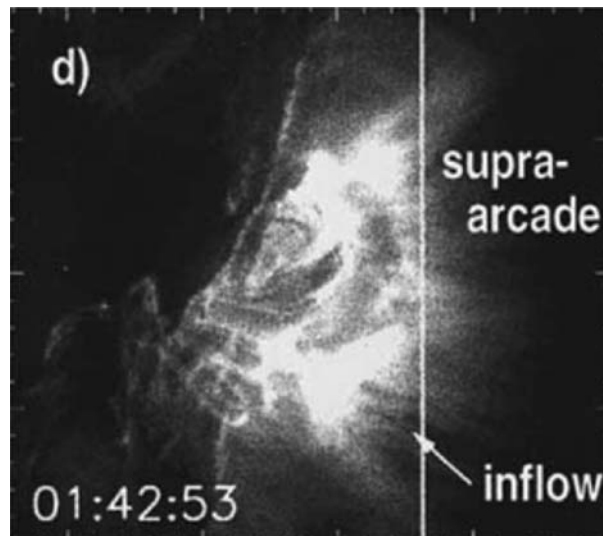

Figure 23. Dark lanes due to downflows as seen in a TRACE image (Innes *et al*., 2003b).

hundred km/s) seem much slower than the super-Alfvénic flows expected from the models, as indicated in Figure 20.

One of the key "benefits" of reconnection in the corona is the conversion of magnetic energy into various other energetic manifestations. An important component of this energy release is the production of energetic particles which then interact with the ambient solar atmosphere to produce radiation signatures at radio, hard X-ray and gamma-ray energies. The relationship between this powerful particle acceleration and magnetic reconnection is not understood theoretically at present. In solar flares, the hard X-rays not only emanate from the chromosphere (the footpoint sources) but also, on occasion, from high up in the corona.

The hard X-ray footpoints exhibit strongly correlated fluctuations implying a common source of particles in an acceleration region high in the corona (e.g., Krucker and Lin, 2002). The geometry implied by the simultaneous and spectrally similar production of hard X-ray photons in the chromosphere points to an energy release at a favorable location in the corona where the free magnetic energy can be tapped. Further support for a relation between particle acceleration and reconnection comes from the discovery of an above-the-loop-top hard X-ray source (Masuda *et al.*, 1994) which suggests the reconnection geometry more directly.

In association with the hard and soft X-ray signatures discussed above, observations in the radio provide important evidence for reconnection in the impulsive phase of solar eruptive events. Radio emission at metric and decimetric frequencies provides direct observations of high energy electrons in the solar corona, with the temporal and frequency behavior of the radio data yielding diagnostic information about the origins of the particles. Recently, Karlický *et al.* (2004) have reported on a rare series of slowly drifting structures (drifting in the sense that the frequency decreases, which means an outward motion through a region of decreasing density) observed during two solar flares in the 0.8–4.5 GHz frequency range. These drifts are thought to map the flare magnetic field reconnection as magnetic plasmoids are formed in an extended current sheet due to tearing processes (see also Kliem *et al.*, 2000). Radio observations may also strengthen the case for reconnection in the erupting solar corona (Aurass *et al.*, 2002).

Finally, strong observational evidence for reconnection comes from the post-eruption emission and dynamics. In particular, the behavior of flare ribbons has provided strong support for the reconnection scenario. The behavior of the outer edges of the ribbons especially has pointed in this direction, since these outer edges exhibit irregular Hα line profiles. Recently SOHO/CDS observations have shown the presence of the required "chromospheric evaporation" directly via EUV spectroscopic imaging (Czaykowska *et al.*, 1999).

5.2. RECONNECTION SUMMARY

The array of coronal and chromospheric manifestations associated with a CME throughout its build-up, initiation and evolution all clearly point to a major

reconfiguration of the magnetic field in the solar corona. The energy required by these manifestations is unarguably provided by the magnetic field, yet we are to date still unable to determine exactly how this energy conversion occurs. Magnetic reconnection, as we presently understand it, seems to provide many of the characteristics required but we are limited both observationally by the extremely small scale on which the reconnection physics occurs and theoretically by the complexity of the reconnection processes in 3D. The many solar signatures presented above are consistent with the general idea of magnetic reconnection playing an important role in CMEs and solar flares. However, even if reconnection occurs as part of the CME process we are still not in a position to determine whether reconnection is required to initiate a CME or whether it results in response to a CME. Before we can state unequivocally that magnetic reconnection plays an important role in the dynamics of an event we need a better understanding of the physics of reconnection in 3D and how it occurs in the magnetic and plasma conditions of the solar corona.

6. Future Observations Needed

6.1. CORONAGRAPHS

Looking into the future, we need to fill in the gaps in our knowledge of CMEs such as their initiation mechanism, their 3-dimensional structure and dynamics, their interaction with the solar wind, and their internal ionization state and elemental composition. Fortunately, efforts are already under way to attack the first two problems. STEREO is planned for launch in 2006. Solar Orbiter and Solar Polar Imager (SPI), two missions currently under study, will allow us to view the corona from viewpoints outside the ecliptic plane. This enables imaging of the entire streamer belt at once, which will immediately answer a number of questions related to interaction of CMEs with the solar wind.

What is further needed are high spatial resolution and high cadence observations at low coronal heights, as close as possible to the solar limb. Because the imaging quality deteriorates and the stray light increases rapidly for small distances from the occulter, future coronagraphs must locate the occulter on long booms (of the order of a few tens of meters) to achieve arcsec resolution for heights $<1.3\ R_\odot$. We know that the initial CME development occurs very rapidly in the low corona (<15 min) and involves plasma at many temperatures. Therefore, progress on the initiation and composition of the CMEs requires both white light and spectroscopic imaging observations at a cadence of about 1 minute and in several coronal and transition region lines. All these requirements point towards large aperture ($\sim$30 cm) instruments (for high throughput), in near Earth orbit (for high telemetry downlink rates) with a significant complement of mechanisms,

filters and polarizers to acquire both white light and spectroscopic imaging observations of the inner corona. Only with such instruments will we be able to build a comprehensive picture of the very complex evolution of the CME in the lower corona.

6.2. EUV TELESCOPES AND SPECTROGRAPHS

Future EUV imaging experiments will require improved spatial resolution and time cadence in order to identify reconnection sites and relate them to CME initiation. To understand the sizes and dynamics, resolutions as high as 10–100 km will be needed. The combination of high spatial resolution and cadence implies a high enough sensitivity to detect a reasonable number of photons per pixel per exposure. Full Sun coverage is important because of the unpredictability of CMEs. Coverage of a broad temperature range is also needed in order to follow the rapidly changing temperatures as plasma is heated and as it cools adiabatically when it is ejected. This requires an adequate number of spectral bands and careful choice of their wavelengths. Temperatures as high as 2×10^7 K are accessible. Major progress on these issues can be expected from the Solar Dynamics Observatory (SDO) mission currently under development.

Future EUV spectral experiments also require high spatial resolution and cadence, though the cadence may not be as high as that achieved by the imaging experiments. Spectral resolution adequate to detect Doppler shifts of a few km/s will provide the third dimension for dynamical studies. The biggest challenge may be obtaining a broad enough spectral range to simultaneously determine densities and compositions over a broad temperature range. While there exist a number of spectral bands that include some density-sensitive line ratios and some lines formed over a broad temperature range, a complete characterization of the CME plasma requires quite a large number of spectral lines. As these lines vary greatly in strength and brightness, a large dynamic range is crucial. In addition, a coronagraphic capability is important for studying CME evolution as the eruption reaches its terminal mass and energy. The next EUV spectrograph planned is the EIS instrument on Solar-B, that is to be launched in late 2006.

6.3. VIEWS FROM MULTIPLE PERSPECTIVES

Our understanding of the CME phenomenon is still hindered by a fundamental observational limitation. Imaging observations are necessarily projections on the plane of the sky. We have no direct knowledge of the 3-dimensional distribution and evolution of the CME plasma along the line of sight. Even the radial propagation direction of the center of mass, a very important quantity for space weather studies cannot be reliably measured and therefore must be inferred indirectly (say from the location of the associated active region). The obvious approach on this problem

is to obtain simultaneous observations from multiple perspectives and invert them using tomography techniques to obtain an estimate of the 3D morphology of an event.

This is precisely the objective of the STEREO mission to be launched in 2006. It consists of two identical spacecraft carrying a complement of EUV full disk imagers, white light coronagraphs and in-situ instruments. The two spacecraft will be placed at 1 AU orbits ahead and behind the Earth, respectively. The scale of solar structures accessible to reconstruction is proportional to the spacecraft separation angle (e.g., Wiegelmann, 2004). Therefore, the continuously changing perspective of the observations from the STEREO spacecraft will allow evaluation of the 3D structure of many solar features, from small scale loops to Earth-directed CMEs. STEREO also carries heliospheric imagers (HI) always observing space all along the Sun-Earth line which will enable us to follow CMEs all the way to the Earth.

6.4. RADIO ARRAYS

Two ground based radio arrays, the Frequency Agile Solar Radio Telescope (FASR) and the Low Frequency Array (LOFAR), together with the space-based Solar Imaging Radio Array (SIRA) are presently being developed or planned to provide images in the frequency range 24 GHz to 30 kHz. FASR, LOFAR and SIRA operating jointly will be able to image electron beams, shocks and CMEs during their propagation through the corona and heliosphere up to 1 AU.

6.5. SOLAR ORBITER

The Solar Orbiter mission presently being studied by ESA (Marsch *et al.*, 2002) will provide the next major step forward in the exploration of the Sun and the heliosphere. It incorporates both a near-Sun and a high-latitude phase.

These are the scientific goals for the mission:

- Determine the properties, dynamics and interactions of plasma, fields and particles in the near-Sun heliosphere;
- Investigate the links between the solar surface, corona and inner heliosphere;
- Explore, at all latitudes, the energetics, dynamics and fine-scale structure of the Sun's magnetized atmosphere;
- Probe the solar dynamo by observing the Sun's high-latitude field, flows and seismic waves.

6.6. THE SENTINEL MISSION

As part of NASA's Living With a Star (LWS) program the planned Sentinel mission will develop the physical understanding necessary to reliably model and predict the

radiation environment for Lunar and Martian missions. Sentinels will accomplish this by discovering the physical conditions and mechanisms that govern heliospheric initiation, propagation and solar connection of those energetic phenomena that adversely affect space exploration and life and society here on Earth.

The Sentinels mission will comprise four spinning spacecraft that will approach the Sun to as close as 0.25 AU. They will be separated in solar longitude such as to allow measuring the spatial extent of shock fronts, CMEs and SEP fluxes. They will be assisted by a far-side Imaging Sentinel spacecraft orbiting at some 120° offset from the Earth. Its set of remote-sensing instruments will provide global solar photospheric magnetic field measurements and coronal plasma density and composition observations. A Near Earth Sentinel is the third component of the mission. Its white light and UV coronagraphic capabilities provide remote sensing of the corona.

6.7. SOLAR POLAR IMAGER

The Solar Polar Imager (SPI) mission uses solar sail propulsion to place a spacecraft in a 0.48 AU circular orbit around the Sun with an inclination of 75°. The rapid 4 month polar orbit and the combined in situ and remote sensing instrument suite allow unprecedented studies of the link between the Sun and the solar wind and solar energetic particles. Moreover, SPI can serve as a pathfinder for a permanent solar polar sentinel for space weather prediction in support of the NASA Vision for Space Exploration.

The feasibility of this most desirable mission hinges upon the success of some new and highly ambitious technical developments that are presently underway.

6.8. THE KUAFU SPACE WEATHER EXPLORER MISSION

KuaFu is an initiative by China for a major scientific space mission. It will be an essential element of the International Living with a Star (ILWS) mission line-up. KuaFu is composed of three spacecraft: KuaFu-A will be located at the L1 libration point between Sun and Earth, and it will have instruments to continuously observe the solar disk in the chromospheric Lyman-alpha and coronal extreme ultraviolet emission, to register CMEs in white-light and Lyman-alpha radiation, and to measure in-situ radio waves, the local solar wind plasma and magnetic field, solar energetic particles, as well as the hard X-ray and Gamma-ray spectrum. KuaFu-B1 and KuaFu-B2 are a satellite pair in an Earth polar orbit chosen to allow continuous (24 hours a day) observation of the northern auroral oval and ring current regions.

KuaFu data will be used for the scientific study of space weather phenomena and to raise the standard of end-to-end observation of the Sun-Earth system.

6.9. Measurements of Magnetic Fields in the Chromosphere and the Corona

The dynamics of the solar atmosphere is governed by the magnetic field. In particular, it determines the coronal structure and dynamics from the upper chromosphere through the corona out into the heliospheric environment. The crucial role played by the magnetic field awards the development of measurement methods an extremely high priority in observational solar physics. However, the magnetic field in the corona is so weak that none of the well-known techniques (e.g., using the Zeeman effect) can easily be applied. Lin *et al.* (2004) report a measurement (using coronal Zeeman magnetometry) of the line-of-sight coronal magnetic field 100 arcsec above an active region implying a flux density of about 4 Gauss. They believe that such measurements will be some of the most exciting new opportunities that the Advanced Technology Solar Telescope (ATST) to be built in a few years time will realize. Using spectropolarimetry of the infrared He I line at 1083 nm, chromospheric vector fields of some tens to hundreds of Gauss (see, e.g., Solanki *et al.*, 2003) have been measured. Comparison with field extrapolations from a photospheric magnetogram showed that a non-linear force-free approximation reproduced the observations best (Wiegelmann *et al.*, 2005). Other techniques for inferring the coronal magnetic fields involve Faraday rotation of polarized solar radiation or radio gyrosynchrotron magnetometry, but these techniques are still developing. At this moment it is not known when such measurements will become available. However, it is clear that quantitative measurements of the magnetic field in the upper solar atmosphere are required to solve several of the burning issues on solar physics.

References

Akmal, A., *et al.*: 2001, *ApJ* **553**, 922.

Asai, A., Yokoyama, T., Shimojo, M., and Shibata, K.: 2004, *ApJ* **605**, L77.

Aurass, H., Vršnak, B., and Mann, G.: 2002a, *A&A* **384**, 273.

Bastian, T. S., and Gary, D. E.: 1997, *JGR* **102**, 14031.

Bastian, T. S., Pick, M., Kerdraon, A., Maia, D., and Vourlidas, A.: 2001, *ApJL* **558**, L65.

Bastian, T. S.: 2003, *Adv. Space Res.* **32**, 2705.

Berger, M.: 1984, *Geophys. Astrophys. Fl. Dyn.* **30**, 79.

Bogod, V. M., Grebinskij, A. S., Opeikina, L. V., and Gelfreikh, G. B.: 1998, *Three-Dimensional Structure of Solar Active Regions*, ASP Conf. Ser. 155, p. 279.

Boischot, A.: 1957, *Comptes Rendus Acad. Sci. Paris* **244**, 1326.

Boischot, A., and Clavelier, B.: 1968, *IAU Symposium 35: Structure and Development of Solar Active Regions*, p. 565

Bothmer, V., and Schwenn, R.: 1996, *Adv. Sp. Res.* **17**, 319.

Brueckner, G. E., Koomen, M. J., and Tousey, R.: 1972, *Sol. Phys.* **24**, 254.

Brueckner, G. E.: 1974, *IAU Symposium* **57**, 333.

Brueckner, G. E., *et al.*: 1995, *Sol. Phys.* **162**, 357.

Burkepile, J. K., Hundhausen, A. J., Stanger, A. L., St. Cyr, O. C., and Seiden, J. A.: 2004, *JGR* **109**, A03101.

Burlaga, L. F., Behannon, K. W., and Klein, L. W.: 1987, *J. Geophys. Res.* **92**, 5725.

Burlaga, L. F., Plunkett, S. P., and St. Cyr., O. C.: 2002, *JGR* **107**, SSH1B.

Canfield, R. C., *et al.*: 1993, *ApJ* **411**, 362.

Canfield, R. C., Hudson, H. S., and McKenzie, D. E.: 1999, *GRL* **26**, 627.

Chen, J., *et al.*: 2000, *Astrophys. J.* **533**, 481.

Ciaravella, A., *et al.*: 1997, *ApJ Lett.* **491**, 59.

Ciaravella, A., *et al.*: 2000, *ApJ* **529**, 575.

Ciaravella, A., Raymond, J. C., Li, J., Reiser, P., Gardner, L. D., Ko, Y.-K., *et al.*: 2002, *ApJ* **575**, 1116.

Ciaravella, A., Raymond, J. C., van Ballegooijen, A., Strachan, L., Vour-lidas, A., Li, J., *et al.*: 2003, *ApJ* **597**, 1118.

Ciaravella, A., Raymond, J. C., Kahler, S., Vourlidas, A., and Li, J.: 2005,*ApJ* **621**, 1121.

Ciaravella, A., Raymond, J. C., and Kahler, S. K.: 2006, *ApJ*, submitted.

Claßen, H. T., Mann, G., Klassen, A., and Aurass, H.: 2003, *A&A* **409**, 309.

Cremades, H., and Bothmer, V.: 2004, *A&A* **422**, 307.

Cremades, H., and Bothmer, V.: 2005, *IAU Symposium* **226**, 48.

Crifo, F., Picat, J. P., and Cailloux, M.: 1983, *Solar Phys.* **83**, 143.

Czaykowska, A., de Pontieu, B., Alexander, D., and Rank, G.: 1999, *ApJL* **521**, L75.

Delaboudiniére, J.-P., Artzner, G. E., Brunaud, J., *et al.*: 1995, *Solar Phys.* **162**, 291.

Démoulin, P., Mandrini, C. H., van Driel-Gesztelyi, L., Thompson, B. J., Plunkett, S., Kovári, Zs., *et al.*: 2002 *A&A* **382**, 650.

Dere, K. P., Wang, D., and Howard, R.: 2005, *ApJL* **620**, L119.

DeVore, C. R.: 2000, *ApJ* **539**, 954.

Dobrzycka, D., Raymond, J. C., Biesecker, D. A., Li, J., and Ciaravella, A.: 2003, *ApJ* **588**, 586.

Domingo, V., *et al.*: 1995, *Sol. Phys.* **162**, 1.

Dulk, G. A., and McLean, D. J.: 1978, *Solar Phys.* **57**, 279.

Erickson, W. C., Kassim, N. E., and Perley, R. A.: 2000, *Radio Astronomy at Long Wavelengths*, p. 303.

Filippov, B., and Koutchmy, S.: 2002, *Sol. Phys.* **208**, 283.

Forbes, T. G., and Acton, L. W.: 1996 *ApJ* **459**, 330.

Forbes, T. G., Linker, J. A., *et al.*: 2006, *Space Sci. Rev.* this volume, 10.1007/s11214-006-9019-8.

Frost, K. J.: 1974, *IAU Symp. 57: Coronal Disturbances*. p. 421.

Gallagher, P. T., Dennis, B. R., Krucker, S., Schwartz, R. A., and Tolbert, A. K.: 2002, *Solar Phys.* **210**, 341.

Gary, D. E., and Hurford, G. J.: 1990, *ApJ* **36**, 290.

Gary, D. E., and Keller, C. U.: 2004, *Solar and Space Weather Radiophysics – Current Status and Future Developments* (Dordrecht: Kluwer).

Gergely, T. E., Kundu, M. R., Munro, R. H., and Poland, A. I.: 1979, *ApJ* **230**, 575.

Gibson, S. E., *et al.*: 2002, *ApJ* **574**, 1021.

Gibson, S. E., and Low, B. C.: 1998, *ApJ* **493**, 460.

Gilbert, H. R., Serex, E. C., Holzer, T. E., MacQueen, R. M., and McIntosh, P. S.: 2001, *ApJ* **550**, 1093.

Gonzalez, W. D., and Tsurutani, B. T.: 1987, *PSS* **35**, 1101.

Gopalswamy, N., and Kundu, M. R.: 1989, *Solar Phys.* **122**, 145.

Gopalswamy, N., and Kundu, M. R.: 1990, *ApJL* **365**, L31.

Gopalswamy, N., and Kundu, M. R.: 1992, *ApJL* **390**, 37.

Gopalswamy, N., Kundu, M. R., Hanaoka, Y., Enome, S., Lemen, J. R., and Akioka, M.: 1996, *New Astron.* **1**, 207.

Gopalswamy, N., Hanaoka, Y., Kundu, M. R., Enome, S., Lemen, J. R., Akioka, M., and Lara, A.: 1997, *ApJ* **475**, 348.

Gopalswamy, N., Nitta, N., Manoharan, P. K., Raoult, A., and Pick, M. 1999, *A&A* **347**, 684.

Gopalswamy, N., Kaiser, M. L. Jones, D. L., and The Alfa Team: 1999, in: T. S. Bastian, N. Gopalswamy and K. Shibasaki, (eds.), *Proceedings of the Nobeyama Symposium*, held in Kiyosato, Japan, Oct. 27-30, 1998, NRO Report No. 479., p. 447.

Gopalswamy, N., and Thompson, B. J.: 2000, *J. Atm. Solar-Terres. Phys.* **62**, 16, 1457.

Gopalswamy, N., *et al.*: 2000a, *Geophys. Res. Lett.* **27**, 145.

Gopalswamy, N. Hanaoka, Y., and Hudson: 2000, *Adv. Space Res.* **25**(9), 1851.

Gopalswamy, N., Yashiro, S., Kaiser, M. L., Howard, R. A., Bougeret, J.-L.: 2001, *ApJ* **548**, L91–L94.

Gopalswamy, N., Yashiro, S., Michalek, G., Kaiser, M. L., Howard, R. A., Reames, D. V., *et al.*: 2002, *ApJ* **572**, L103–L107.

Gopalswamy, N., *et al.*: 2003, *GRL* **30**(12), SEP 3–1.

Gopalswamy, N., Lara, A., Yashiro, S., and Howard, R. A.: 2003b, *ApJ* **598**, L63.

Gopalswamy, N.: 2004a, in: Poletto, G., and Suess, S. (ed.), *The Sun and the Heliosphere as an Integrated System*, ASSL series, (Kluwer: Boston), p. 201.

Gopalswamy, N., Yashiro, S., Krucker, S., Stenborg, G., and Howard, R. A.: 2004, *J. Geophys. Res.* **109**, 12105.

Gopalswamy, N., Yashiro, S., Krucker, S., and Howard, R.A: 2005, in: Dere, K. P., Wang, J., and Yan, Y. (eds.), *Coronal and Stellar Mass Ejections*, International Astronomical Union, p. 367.

Gopalswamy, N., Yashiro, S., Liu, Y., Michalek, G., Vourlidas, A., Kaiser, M. L., *et al.*: 2005a, *J. Geophys. Res.* **110**, A09S15.

Gopalswamy, N., Fleck, B., and Gurman, J. B.: 2005b, in: Rao, M., and Murthy, R. L. N. (eds.),*IAA "Bringing Space Benefits to the Asia Region"* (Bangalore: Asronautical Society of India).

Gopalswamy, N., Mikić, Z., *et al.*: 2006, *Space Science Reviews*, this volume, 10.1007/s11214-006-9020-2.

Gosling, J. T., Birn, J., and Hesse, M.: 1995, *GRL* **22**, 869.

Green, L. M., López Fuentes, M. C., Mandrini, C. H., Démoulin, P., Van Driel-Gesztelyi, L., Culhane, J. L.: 2002, *Sol. Phys.* **208**, 43.

Habbal, S. R., Mossman, A., Gonzalez, R., and Esser, R.: 1996, *JGR* **101**, 19943.

Hanaoka, Y., *et al.*: 1994 *PASJ* **46**, 205.

Handy, B. N., *et al.*: 1999, *Sol. Phys.* **187**, 229.

Harrison, R. A.: 1986, *A&A* **162**, 283.

Harrison, R. A.: 2003, *Adv. Sp. Res.* **32**, 2425.

Harrison, R. A., *et al.*: 1995, *Sol. Phys.* **162**, 233.

Harvey, J. W., and Sheeley, N. R.: 1979, *SSRv* **23**, 139.

Hill, S. M., *et al.*: 2005, *Sol. Phys.* **226**, 255.

Howard, R. A., Michels, D. J., Sheeley, N. R., Jr., and Koomen, M. J.: 1982, *Astrophys. J.* **263**, L101.

Howard, R. A., *et al.*: 1985, *JGR* **90**, 8173.

Howard, R. A., *et al.*: 1997, in: Crooker, N., Joselyn, J., and Feynman, J. (eds.), *Coronal Mass Ejections*, (Washington DC: Amer. Geophys. Union), p. 17.

Howard, R. A., Moses, J. D., Socker, D. G., Dere, K. P., and Cook, J. W.: 2002, *Adv. Sp. Res.* **29**(12), 2017.

Hudson, H. S., Acton, L. W., and Friedland, S. L.: 1996, *ApJ* **470**, 629.

Hudson, H. S., Acton, L. W., Harvey, K. L., and McKenzie, D. E.: 1999, *ApJL* **513**, L83.

Hundhausen, A. J.: 1985, in: Stone, R. G., and Tsurutani, B. T. (eds.), *Collisionless Shocks in the Heliosphere, A Tutorial Review*, (Washington: AGU), p. 37.

Hundhausen, A. J.: 1987, *Sixth International Solar Wind Conference*, p. 181.

Hundhausen, A. J.: 1993, *JGR* **98**, 13177.

Illing, R. M. E., and Hundhausen, A. J.: 1983, *J. Geophys. Res.* **88**, 10,210.

Innes, D. E., Curdt, W., Schwenn, R., Solanki, S., Stenborg, G., and McKenzie, D. E.: 2001, *ApJL* **549**, L249.

Innes, D. E., McKenzie, D. E., and Wang, T.: 2003a, *Sol. Phys.* **217**, 267.

Innes, D. E., McKenzie, D. E., and Wang, T.: 2003b, *Sol. Phys.* **217**, 247.

Irimajiri, Y., Takano, T., Nakajima, H., Shibaska, K., Hanaoka, Y., and Ichimoto, K.: 1995, *Sol. Phys.* **156**, 363.

Kahler, S. W.: 1992, *Ann. Revs. Astron. Ap.* **30**, 113.

Kahler, S. W., and Hudson, H. S.: 2001, *JGR* **106**, 29,239.

Kahler, S. W., and Hundhausen, A. J.: 1992, *JGR* **97**, 1619.

Kahler, S. W.: 2001, *J. Geophys. Res.* **106**, 20947.

Kallenrode, M.-B., and Cliver, E. W.: 2001, *Proceedings of the ICRC 2001*, 3318.

Karlický, M., Fárnik, F., and Krucker, S.: 2004, *A&A* **419**, 365.

Kathiravan, C., Ramesh, R., and Subramanian, K. R.: 2002, *ApJL* **567**, L93.

Kaufmann, P., *et al.*: 2001, in: Pinho, J. T., Santos Cavalcante, G. P., and Oliveira, L. A. H. G. (eds.), *Proc. SBMO/IEEE MTT-S Int. Microwave and Optoelectronic Conf.*, (Piscataway, IEEE), p. 439.

Kaufmann, P., *et al.*: 2003, *J. Geophys. Res.* **108**, 1280.

Kerdraon, A., Pick, M., Trottet, G., Sawyer, C., Illing, R., Wagner, W., *et al.*: 1983, *ApJL* **265**, L19.

Kerdraon, A., and Delouis, J.: 1997, in: Trottet, G. (ed.), *Coronal Phsyics from Radio and Space Observations; Proceedings of the CESRA Workshop held in Nouan le Fuzelier*, (Berlin: Springer Verlag), p. 192.

Khan, J. I., and Hudson, H. S.: 2000, *GRL* **27**, 1083.

Kiplinger, A. L.: 1995, *ApJ* **453**, 973.

Kliem, B., Karlický, M., and Benz, A. O.: 2000, *A&A* **360**, 715.

Ko, Y.-K., Raymond, J. C., Lin, J., Lawrence, G., Li, J., and Fludra, A.: 2003, *ApJ* **594**, 1068.

Kohl, J., *et al.*: 1995, *Sol. Phys.* **162**, 313.

Kopp, R. A., and Pneuman, G. W.: 1976, *Sol. Phys.* **50**, 85.

Krucker, S., and Lin, R.: 2002, *Sol. Phys.* **210**, 229.

Krucker, S., Christe, S., Lin, R. P., Hurford, G. J., and Schwartz, R. A.: 2002, *Sol. Phys.* **210**, 445.

Kundu, M. R.: 1965, *Solar Radio Astronomy*, (New York: Interscience Publication).

Kusano, K., Maeshiro, T., Yokoyama, T., and Sakurai, T.: 2002, *ApJ* **577**, 501.

Lantos, P., Kerdraon, A., Rapley, C. G., and Bentley, R. D.: 1981, *A&A* **101**, 33.

Lara, A., Gopalswamy, N., Caballero-Lopez, R., Yashiro, S., and Valdes-Galicia, J.: 2005, *ApJ* **625**, 441.

Leamon, R. J., Canfield, R. C., and Pevtsov, A. A.: 2002, *JGR* **107**, SSH1.

Lee, J.-Y., Raymond, J. C., Ko, Y.-K., and Kim, K.-S.: 2006, *ApJ*, submitted.

Li, G., and Zank, G. P.: 2005, *GRL* **32**, L02101.

Lin, H., Kuhn, J. R., and Coulter, R.: 2004, *ApJ* **613**, L177.

Lin, J.: 2002, *ChJAA* **2**, 539.

Lin, J., and Forbes, T. G.: 2000, *JGR* **105**, 2375.

Lin, J., Raymond, J. C., and van Ballegooijen, A. A.: 2004, *ApJ* **602**, 422.

Lin, J., Ko, Y.-K., Sui, L., Raymond, J. C., Stenborg, G. A., Jiang, Y., *et al.*: 2005, *ApJ* **622**, 1251.

Lin, R. P., Dennis, B. R., Hurford, G. J., and 63 co-authors: 2002, *Solar Phys.* **210**, 3.

Linker, J., *et al.*: 1999, *JGR* **104**, 9809.

Linker, J., Lionello, R., Mikić and Amari, T.: 2001, *JGR* **106**, 25165.

Low, B.-C.: 1982, *ApJ* **254**, 796.

Low, B.-C.: 1984, *ApJ* **281**, 392.

Low, B.-C.: 1996, *Sol. Phys.* **167**, 217.

Low, B.-C.: 2001, *JGR* **106**, 25,141.

Luhmann, J. G., Li, Y., Zhao, X., and Yashiro, S.: 2003, *Solar Phys.* **213**, 367.

Mancuso, S., Raymond, J. C., Kohl, J., Ko, Y.-K., Uzzo, M., and Wu, R.: 2002, *A&A* **383**, 267.

Marqué, C.: 2004, *ApJ* **602**, 1037.

Martin, S. F., and McAllister, A. H.: 1996, *Magnetodynamic Phenomena in the Solar Atmosphere - Prototypes of Stellar Magnetic Activity*, IAU Colloq. 153, p. 497.

Marsch, E., Antonucci, E., Bochsler, P., Bougeret, J.-L., Fleck, B., Harrison, R., *et al.*: 2002, *Adv. Sp. Res.* **29**, 2027.

Masuda, S., Kosugi, T., Hara, H., Tsuneta, S., and Ogawara, Y.: 1994, *Nature* **371**, 495.

McKenzie, D. E., and Hudson, H. S.: 1999, *ApJ* **519**, L93.

McKenzie, D. E.: 2000, *Sol. Phys.* **195**, 381.

Metcalf, T. R., Jiao, L., McClymont, A. N., Canfield, R. C., and Uitenbroek, H.: 1995, *ApJ* **439**, 474.

Milkey, D. L., Canfield, R. C., Labonte, B. j., Leka, K. D., Waterson, M. F., and Weber, H. M.: 1996, *Sol. Phys.* **168**, 229.

Moon, Y.-J., Choe, G. S., Wang, H. M., Park, Y. D., Gopalswamy, N., Yang, G., *et al.*: 2002, *ApJ* **581**, 694.

Moran, T., and Davila, J.: 2004, *Science* **305**, 66.

Moreton, G. E., and Ramsey, H. E.: 1960, *PASP* **72**, 357.

Moses, D. Clette, F., Delabouniniere, J.-P., and 32 co-authors: 1997, *Sol. Phys.* **175**, 571.

Munro, R. H., *et al.*: 1979, *Solar Phys.* **61**, 201.

Nakajima *et al.*: 1994, *Proceedings of Kofu Symposium*, Kofu, Japan, Sept. 6–10, 1993, p. 185.

Nindos, A., and Zhang, H.: 2002, *ApJL* **573**, 133.

Panasyuk, A.: 1999, *JGR* **104**, 9721.

Parker, E. N.: 1961, in: Liller, W. (ed.), *Space Astrophysics*, (New York: McGraw-Hill), p. 157.

Parker, E. N.: 1963, in: Evans, J. W. (ed.), *Proceedings of IAU Symposium 16*, (New York: Academic Press), p. 11.

Payne-Scott, R., Yabsley D. E., and Bolton, J. G.: 1947, *Nature* **160**, 256.

Pick, M.: 1986, *Solar Phys.* **104**, 19.

Pick, M., Démoulin, P., Krucker, S., Malandraki, O., and Maia, D.: 2005, *ApJ* **625**, 1019.

Pick, M., Forbes, T. G., Mann, G., *et al.*: 2006, *Space Science Reviews*, this volume, 10.1007/s11214-006-9021-1.

Plunkett, S. P., *et al.*: 1998, *GRL* **25**, 2477.

Plunkett, S. P., *et al.*: 2000, *Solar Phys.* **61**, 201.

Pohjolainen, S., Maia, D., Pick, M., *et al.*: 2001, *Astrophys. J.* **556**, 421.

Ramaty, R., and Lingenfelter, R. E.: 1967, *JGR* **72**, 879.

Ramesh, R., Subramanian, K. R., Sundararajan, M. S., and Sastry, C. V.: 1998, *Sol. Phys.* **181**, 439.

Rao, A. P., Ananthakrishnan, S., Balasubramanian, V., and Coles, W. A.: 1995, *Solar Wind* **8**, 94.

Raouafi, N.-E., Mancuso, S., Solanki, S. K., Inhester, B., Mierla, M., Stenborg, G., *et al.*: 2004, *A&A* **424**, 1039.

Raymond, J. C., Thompson, B. J., St. Cyr, O. C., Gopalswamy, N., Kahler, S., Kaiser, M., *et al.*: 2000, *GRL* **27**, 1439.

Raymond, J. C., Ciaravella, A., Dobrzycka, D., Strachan, L., Ko, Y.-K., Uzzo, M., *et al.*: 2003, *ApJ* **597**, 1106.

Raymond, J. C., and Ciaravella, A.: 2004, *ApJL* **606**, L159.

Riddle, A. C.: 1970, *Sol. Phys.* **13**, 448.

Robinson, R. D.: 1985, *Solar Radiophysics: Studies of Emission from the Sun at Metre Wavelengths*, p. 385.

Rust, D. M.: 1983, *SSRv* **34**, 21.

Rust, D. M., and Kumar, A.: 1994, *Sol. Phys.* **155**, 69.

Rust, D. M.: 2001, *JGR* **106**, 25,075.

Sakurai, T., Shibata, K., Ichimoto, K., Tsuneta, S., and Acton, L. W.: 1992, *PASJ* **44**, 123.

Scherrer, P. H., *et al.*: 1995, *Sol. Phys.* **162**, 129.

Schwenn, R.: 1986, *Space Sci. Rev.* **44**, 139.

Schwenn, R., dal Lago, A., Huttunen, E., and Gonzales, W. D.: 2005, *Ann. Geophys.* **23**, 1033.

Sheeley, N. R., Howard, R. A., Koomen, M. J., and Michels, D. J.: 1983, *ApJ* **272**, 349.

Sheeley, N. R., Jr., Wang, Y.-M., Hawley, S. H., and other 15 authors: 1997, *ApJ* **484**, 472.

Sheeley, N. R., Jr., Walters, J. H., Wang, Y.-M, and Howard, R. A.: 1999, *JGR* **104**, 24,739.

Sheeley, N. R., Jr., Hakala, W. N., and Wang, Y.-M.: 2000, *JGR* **103**, 5081.

Sheeley, N. R., Jr., and Wang, Y.-M.: 2002, *ApJ* **579**, 874.

Sheridan, K. V.: 1970, *Proceedings of the Astronomical Society of Australia* **1**, 376.

Sime, D. G., and Hundhausen, A. J.: 1987, *JGR* **92**, 1049.

Simon, M., and Axford, W. I.: 1966, *PSS* **14**, 901.

Skumanich, A., Lites, B. W., Martinez, P. V., and Seagraves, P.: 1997, *ApJS* **110**, 357.

Smith, S. F., and Harvey, K. L.: 1971, in: Macris, C. J. (ed.) *Physics of the Solar Corona*, p. 156.

Solanki, S. K., Lagg, A., Woch, J., Krupp, N., and Collados, M.: 2003, *Nature* **425**, 692.

Spirock, T. J., Denker, C., Varsik, J., Shumko, S., Qiu, J., Gallagher, P., *et al.*: 2001, *AGUSM*, SP51B-06.

Srivastava, N., Schwenn, R., Inhester, B., Stenborg, G., and Podlipnik, B.: 1999, *Space. Sci. Rev.* **87**, 303.

Srivastava, N., Schwenn, R., Inhester, B., Martin, S. F., and Hanaoka, Y.: 2000, *ApJ* **534**, 468.

St. Cyr, O. C., *et al.*: 2000, *J. Geophys. Res.* **105**, 18,169.

Stenborg, G., Bagalá. L. G., Bauer, O. H., Borda, R. F., Francile, C., Haerendel, G., Rovira, M. G., *et al.*: 2000, *J. Atmos. Terrest. Phys.* **62**, 1553.

Sterling, A. C., and Hudson, H. S.: 1997, *ApJL* **491**, 55.

Sterling, A. C., Hudson, H. S., Thompson, B. J., and Zarro, D. M.: 2000, *ApJ* **532**, 628.

Stewart, R. T.: 1985, *Solar Radiophysics: Studies of Emission from the Sun at Metre Wavelengths*, p. 361.

Sui, L., and Holman, G. D.: 2003, *ApJL* **596**, L251.

Swarup, G.: 2000, *Radio Astronomy at Long Wavelengths*. p. 297.

Tandberg-Hanssen, E.: 1995, *The Nature of Solar Prominences* (Kluwer, Dordrecht).

Thompson, B. J., Plunkett, S. P., Gurman, J. B., Newmark, J. S., St. Cyr, O. C., and Michels, D. J.: 1998, *Geophys. Res. Lett.* **25**, 2465.

Thompson, B. J., *et al.*: 1999, *Astrophys. J.* **517**, L151.

Tripathi, D., Bothmer, V., and Cremades, H.: 2004, *ApJ* **422**, 337.

Tripathi, D., Solanki, S. K., Schwenn, R., *et al.*: 2006, *A&A*, in press.

Tsuneta, S.: 1996, *ApJ* **456**, 840.

Tsuneta, S., Hara, H., Shimizu, T., Acton, L. W., Strong, K. T., Hudson, H. S., and Ogawara, Y.: 1992, *PASJ* **44**, L63.

Vaiana, G. S., Davis, J. M., Giacconi, R., Krieger, A. S., Silk, J. K., Timothy, A. F., *et al.*: 1973, *ApJL* **185**, L47.

Vourlidas, A., *et al.*: 2002, in: Wilson, A. (ed.), *Solar Variability: From Core to Outer Frontiers*. 10th Eur. Sol. Phys. Mtg, Prague, Czech Republic. ESA SP-506, Vol. 1. Noordwijk: ESA Publications Division, p. 91.

Vourlidas, A., Subramanian, P., Dere, K. P., and Howard, R. A.: 2000, *ApJ* **534**, 456.

Vourlidas, A., Wu, S. T., Wang, A. H., Subramanian, P., and Howard, R. A.: 2003, *ApJ* **598**, 1392.

Wang, Y.-M., Sheeley, N. R., Jr., Howard, R. A., St. Cyr. O. C., and Simnett, G. M.: 1999, *Geophys. Res. Lett.* **26**, 1203.

Wang, Y.-M., and Sheeley, N. R. Jr.: 2002a, *ApJ* **567**, 1211.

Wang, Y.-M., and Sheeley, N. R. Jr.: 2002b, *ApJ* **575**, 542.

Webb, D. F., and Hundhausen, A. J.: 1987, *Sol. Phys.* **108**, 383.

Webb, D. F., Burkepile, J., Forbes, T. G., and Riley, P.: 2003, *JGR* **108**, SSH6-1.

Wiegelmann, T.: 2004, *Sol. Phys.* **219**, 87.

Wiegelmann, T., Lagg, A., Solanki, S. K., Inhester, B., and Woch, J.: 2005, *Astron. Astrophys.* **433**, 701.

White, S., Kassim, N. E., and Erickson, W. C.: 2003, in: Keil, S. L., and Avakyan, S. V. (eds.), *Innovative Telescopes and Instrumentation for Solar Astrophysics. Proceedings of the SPIE, Volume 4853*, p. 111.

Wiik, J. E., *et al.*: 1997, *Sol. Phys.* **175**, 411.

Wild, J. P.: 1969, *Sol. Phys.* **9**, 260.

Wilhelm, K., *et al.*: 1995, *Sol. Phys.* **162**, 189.

Yashiro, S., Gopalswamy, N., Michalek, G., and Howard, R. A.: 2003, *Adv. Space Res.* **32**, 2631.

Yashiro, S., Gopalswamy, N., Michalek, G., St. Cyr, O. C., Plunkett, S. P., Rich, N. B., *et al.*: 2004, *JGR* **109**, A07105.

Yokoyama, T., Akita, K., Morimoto, T., Inoue, K., and Newmark, J.: 2001, *ApJL* **546**, L69.

Zandanov, V. G., Altyntsev, A. T., and Lesovoi, S. V.: 1999, in: Bastian, T. S., Gopalswamy, N., and Shibasaki, K. (eds.), *Proceedings of the Nobeyama Symposium, Held in Kiyosato, Japan, Oct. 27-30, 1998*, NRO Report No. 479., p.425–428. p. 425.

Zhang, J., Dere, K. P., Howard, R. A., Kundu, M. R., and White, S. M.: 2001, *ApJ* **559**, 452.

Zhang, J., Dere, K. P., Howard, R. A., and Vourlidas, A.: 2004, *ApJ* **604**, 420.

Zhitnik, I., *et al.*: 2003a, *MNRAS* **338**, 67.

Zhitnik, I., *et al.*: 2003b, *Adv. Sp. Res.* **32**(12), 2573.